IMPRINT OF REIONIZATION ON THE COSMIC MICROWAVE BACKGROUND BISPECTRUM

ASANTHA COORAY[1] AND WAYNE HU[2]

ABSTRACT

We study contributions to the cosmic microwave background (CMB) bispectrum from non-Gaussianity induced by secondary anisotropies during reionization. Large-scale structure in the reionized epoch both gravitationally lenses CMB photons and produces Doppler shifts in their temperature from scattering off electrons in infall. The resulting correlation is potentially observable through the CMB bispectrum. The second-order Ostriker-Vishniac effect also couples to a variety of linear secondary effects to produce a bispectrum. For the currently favored flat cosmological model with a low matter content and small optical depth in the reionized epoch $\tau \lesssim 0.3$, however, these bispectrum contributions are well below the detection threshold of *MAP* and at or below that of *Planck*, given their cosmic and noise variance limitations. At the upper end of this range, they can serve as an extra source of noise for measurements with *Planck* of either primordial nongaussianity or that induced by the correlation of gravitational lensing with the integrated Sachs-Wolfe and the thermal Sunyaev-Zel'dovich effects. We include a discussion of the general properties of the CMB bispectrum, its configuration dependence for the various effects, and its computation in the Limber approximation and beyond.

Subject headings: cosmic microwave background — cosmology: theory — large-scale structure of universe — gravitational lensing

1. INTRODUCTION

The increase in sensitivity of upcoming cosmic microwave background (CMB) experiments, especially satellite missions, raises the possibility that higher order correlations in the CMB temperature fluctuations, beyond the two-point function, may be experimentally detected and studied in detail to look for deviations from Gaussianity. In the absence deviations in the initial conditions, they may arise from the imprint of the nonlinear growth of structures on secondary anisotropies.

Early theoretical work on the three-point correlation function was aimed at distinguishing between various theories of the origin of the fluctuations (e.g., Falk, Rangarajan, & Frednicki 1993; Luo & Schramm 1993; Luo 1994; Gangui et al 1994). Within the context of inflationary models, especially within slow-roll inflation, this topic has been further addressed in several recent papers (e.g., Gangui & Martin 2000; Wang & Kamionkowski 2000). In typical models, the expected non-Gaussian contribution is below the level that can be detected owing to cosmic variance limitations.

Recently, there has been much renewed interest in the three-point function and its Fourier analogue the bispectrum, both in anticipation of the high-precision satellite data and from analyses of the *COBE* DMR data (e.g., Hinshaw et al 1995; Ferreira, Manguiijo, & Gorski 1998; Pando, Vallas-Gabaud, & Fang 1998). The detection reported by Ferreira et al. (1998) and Pando et al. (1998) has been subsequently shown to be associated with a known systematic error in the data time-stream (Banday, Zaroubi, & Gorski 1999; see also Bromley & Tegmark 1999). This should be taken as a cautionary tale that even if an experiment has the raw sensitivity to detect expected bispectrum

signals, removing systematic effects to the required level will prove challenging indeed.

Nonetheless, the upcoming CMB experiments, especially *MAP*[3] and *Planck* surveyor,[4] with their higher sensitivity and angular resolution can in principle be used to study the bispectrum. It is therefore important to investigate what signals are expected in the currently favored cosmological models and how they might be separated from each other. Recently Spergel & Goldberg (1999) and Goldberg & Spergel (1999) studied the CMB bispectrum under the context of non-Gaussian contribution due to second-order gravitational effects, notably the correlation induced by gravitational lensing of CMB photons and secondary anisotropies from the integrated Sachs-Wolfe (ISW; Sachs & Wolfe 1967) effect and the thermal Sunyaev-Zel'dovich (SZ; Sunyaev & Zel'dovich 1980) effect.

Here we present two additional effects resulting through reionization. The first one is the correlation induced by lensing through the secondary Doppler effect. The second one arises from the coupling of the second order Ostriker-Vishniac effect (OV; Ostriker & Vishniac 1986; Vishniac 1987) to other linear secondary effects such as the ISW, Doppler, and SZ effects. The resulting bispectrum is proportional to the square of the matter density power spectra. We also study the configuration dependence of these effects to address means by which they may be separated from each other and any primordial nongaussianity.

The layout of the paper is as follows. In § 2, we review the background material relevant for understanding the CMB bispectrum and its statistical properties in the context of the adiabatic cold dark matter (CDM) models. A summary of useful properties of the Wigner-3j symbol is presented in the Appendix. In § 3, we detail the coupling between gravitational lensing angular excursions and secondary anisotropies. Results for the currently favored cosmology are

[1] Department of Astronomy and Astrophysics, University of Chicago, Chicago IL 60637.

[2] Institute for Advanced Study, Princeton, NJ 08540; asante@hyde.uchicago.edu, whu@ias.edu.

presented in § 4. In § 5, we treat the coupling between Ostriker-Vishniac (OV) effect and secondary temperature fluctuations; results for the favored cosmological model are presented in § 6. We conclude in § 7.

2. PRELIMINARIES

We first review the properties of adiabatic CDM models relevant to the present calculations. We then discuss the general properties of the angular bispectrum of the CMB.

2.1. *Adiabatic CDM Model*

The expansion rate for adiabatic CDM cosmological models with a cosmological constant is

$$H^2 = H_0^2[\Omega_m(1 + z)^3 + \Omega_K(1 + z)^2 + \Omega_\Lambda] , \qquad (1)$$

where H_0 can be written as the inverse Hubble distance today, $H_0^{-1} = 2997.9h^{-1}$Mpc. We follow the conventions that in units of the critical density $3H_0^2/8\pi G$, the contribution of each component is denoted Ω_i, $i = c$ for the CDM, b for the baryons, Λ for the cosmological constant. We also define the auxiliary quantities $\Omega_m = \Omega_c + \Omega_b$ and $\Omega_K = 1 - \sum_i \Omega_i$, which represent the matter density and the contribution of spatial curvature to the expansion rate, respectively.

Convenient measures of distance and time include the conformal distance (or look-back time) from the observer at redshift $z = 0$

$$r(z) = \int_0^z \frac{dz'}{H(z')} , \qquad (2)$$

and the analogous angular diameter distance

$$d_A = H_0^{-1} \Omega_K^{-1/2} \sinh (H_0 \Omega_K^{1/2} r) . \qquad (3)$$

Note that as $\Omega_K \to 0$, $d_A \to r$ and we define $r(z = \infty) = r_0$.

The adiabatic CDM model possesses a power spectrum of density fluctuations

$$\langle \delta(\boldsymbol{k})^* \delta(\boldsymbol{k}') \rangle = (2\pi)^3 \delta^D(\boldsymbol{k} - \boldsymbol{k}') \frac{2\pi^2}{k^3} \Delta^2(k) , \qquad (4)$$

where δ^D is the Dirac delta function[5] and

$$\Delta^2(k) = \delta_H^2 \left(\frac{k}{H_0}\right)^{n+3} T^2(k) , \qquad (5)$$

in linear perturbation theory. We use the fitting formulae of Eisenstein & Hu (1999) in evaluating the transfer function $T(k)$ for CDM models. Here δ_H is the amplitude of present-day density fluctuations at the Hubble scale; we adopt the *COBE* normalization for δ_H (Bunn & White 1997).

The density field may be scaled backward to higher redshift by the use of the growth function $G(z)$, where $\delta(k, r) = G(r)\delta(k,0)$ (Peebles 1980), and

$$G(r) \propto \frac{H(r)}{H_0} \int_{z(r)}^\infty dz'(1 + z') \left(\frac{H_0}{H(z')}\right)^3 . \qquad (6)$$

Note that in the matter dominated epoch $G \propto a = (1 + z)^{-1}$; it is therefore convenient to define an auxiliary quantity $F \equiv G/a$.

---

[5] We also use this symbol for Kronecker deltas.

The cosmological Poisson equation relates the density field to the fluctuations in the gravitational potential

$$\Phi = \frac{3}{2} \Omega_m \left(\frac{H_0}{k}\right)^2 \left(1 + 3 \frac{H_0^2}{k^2} \Omega_K\right)^{-2} F(r)\delta(k, 0) . \qquad (7)$$

Likewise, the continuity equation relates the density and velocity fields via

$$\boldsymbol{v} = -i\dot{G}\delta(k, 0) \frac{\boldsymbol{k}}{k^2} , \qquad (8)$$

where overdots represent derivatives with respect to radial distance r.

For fluctuation spectra and growth rates of interest here, reionization of the universe is expected to occur rather late, $z_{\rm ri} \lesssim 50$, such that the reionized media is optically thin to Thomson scattering of CMB photons $\tau \lesssim 1$. The probability of last scattering within dr of r (the visibility function) is

$$g = \dot{\tau}e^{-\tau} = XH_0 \tau_H(1 + z)^2 e^{-\tau} . \qquad (9)$$

Here $\tau(r) = \int_0^r dr\dot{\tau}$ is the optical depth out to r, X is the ionization fraction, and

$$\tau_H = 0.0691(1 - Y_p)\Omega_b h , \qquad (10)$$

is the optical depth to Thomson scattering to the Hubble distance today, assuming full hydrogen ionization with primordial helium fraction of Y_p. Note that the ionization fraction can exceed unity: $X = (1 - 3Y_p/4)/(1 - Y_p)$ for singly ionized helium, and $X = (1 - Y_p/2)/(1 - Y_p)$ for fully ionized helium. We assume that

$$X(z) = 1 - \frac{1}{2} \operatorname{erfc}\left(\frac{z_{\rm ri} - z}{\sqrt{2}\Delta z}\right) \qquad (11)$$

such that hydrogen reionizes smoothly but promptly at $z_{\rm ri}$; some aspects of the Doppler effect, in particular its power spectrum and to a lesser extent Doppler-Doppler-OV coupling, are sensitive to the sharpness of this transition.

Although we maintain generality in all derivations, we illustrate our results with the currently favored ΛCDM cosmological model. The parameters for this model are $\Omega_c = 0.30$, $\Omega_b = 0.05$, $\Omega_\Lambda = 0.65$, $h = 0.65$, $Y_p = 0.24$, $n = 1$, and $\delta_H = 4.2 \times 10^{-5}$. This model has mass fluctuations on the $8h$ Mpc^{-1} scale in accord with the abundance of galaxy clusters $\sigma_8 = 0.86$. A reasonable value here is important since the bispectrum is nonlinearly dependent on the amplitude of the density field. We consider reionization redshifts in the range $5 \lesssim z_{\rm ri} \lesssim 40$ or $0.025 \lesssim \tau \lesssim 0.5$ and assume $\Delta z/(1 + z) = 0.1$.

2.2. *Bispectrum*

The bispectrum $B_{l_1 l_2 l_3}$ is the spherical harmonic transform of the three-point correlation function just as the angular power spectrum C_ℓ is the transform of the two-point function. In terms of the multipole moments of the temperature fluctuation field $T(\hat{\boldsymbol{n}})$,

$$a_{lm} = \int d\hat{\boldsymbol{n}} T(\hat{\boldsymbol{n}}) Y_l^{m*}(\hat{\boldsymbol{n}}) , \qquad (12)$$

the two-point correlation function is given by

$$C(\hat{\boldsymbol{n}}, \hat{\boldsymbol{m}}) \equiv \langle T(\hat{\boldsymbol{n}})T(\hat{\boldsymbol{m}}) \rangle$$

$$= \sum_{m_1 l_2 m_3} \langle a_{l_1 m_1}^* a_{l_2 m_2} \rangle Y_l^{m*}(\hat{\boldsymbol{n}}) Y_l^m(\hat{\boldsymbol{m}}) . \qquad (13)$$

Under the assumption that the temperature field is statistically isotropic, the correlation is independent of m,

$$\langle a^*_{l_1 m_1} a_{l_2 m_2}\rangle = \delta^D_{l_1 l_2} \delta^D_{m_1 m_2} C_{l_1} , \tag{14}$$

and called the angular power spectrum. Likewise the three-point correlation function is given by

$$B(\hat{n}, \hat{m}, \hat{l}) \equiv \langle T(\hat{n})T(\hat{m})T(\hat{l})\rangle$$
$$\equiv \sum B_{l_1 l_2 l_3}\langle a_{l_1 m_1} a_{l_2 m_2} a_{l_3 m_3}\rangle$$
$$\times Y^{m_1}_{l_1}(\hat{n})Y^{m_2}_{l_2}(\hat{m})Y^{m_3}_{l_3}(\hat{l}) , \tag{15}$$

where the sum is over $(l_1, m_1),(l_2, m_2),(l_3, m_3)$. Statistical isotropy again allows us to express the correlation in terms an m-independent function,

$$\langle a_{l_1 m_1} a_{l_2 m_2} a_{l_3 m_3}\rangle = \begin{pmatrix} l_1 & l_2 & l_3 \\ m_1 & m_2 & m_3 \end{pmatrix} B_{l_1 l_2 l_3} . \tag{16}$$

Here the quantity in parentheses is the Wigner-$3j$ symbol. Its orthonormality relation equation (A2) implies

$$B_{l_1 l_2 l_3} = \sum_{m_1 m_2 m_3} \begin{pmatrix} l_1 & l_2 & l_3 \\ m_1 & m_2 & m_3 \end{pmatrix}\langle a_{l_1 m_1} a_{l_2 m_2} a_{l_3 m_3}\rangle . \tag{17}$$

The angular bispectrum, $B_{l_1 l_2 l_3}$, contains all the information available in the three-point correlation function. For example, the skewness, the collapsed three-point function of Hinshaw et al (1995), and the equilateral configuration statistic of Ferreira et al. (1998) can all be expressed as linear combinations of the bispectrum terms (see Gangui et al 1994 for explicit expressions).

It is also useful to note its relation to the bispectrum defined on a small flat section of the sky. In the flat sky approximation, the spherical polar coordinates (θ, ϕ) are replaced with radial coordinates on a plane ($r = 2 \sin \theta/2 \approx \theta, \phi$). The Fourier variable conjugate to these coordinates is a two-dimensional vector l of length l and azimuthal angle ϕ_l. The expansion coefficients of the Fourier transform of a given l is a weighted sum over m of the spherical harmonic moments of the same l (White et al. 1999)

$$a(l) = \sqrt{\frac{4\pi}{2l+1}} \sum_m i^{-m} a_{lm} e^{im\phi_l} , \tag{18}$$

so that

$$\langle a^*(l_1)a(l_2)\rangle = \frac{2\pi}{l_1} \delta^D_{l_1,l_2} C_{l_1} \sum_m e^{im(\phi_{l_1} - \phi_{l_2})}$$
$$\approx (2\pi)^2 \delta^D(l_1 + l_2)C_{l_1} . \tag{19}$$

Likewise, the two-dimensional bispectrum is defined as

$$\langle a(l_1)a(l_2)a(l_3)\rangle \equiv (2\pi)^2 \delta^D(l_1 + l_2 + l_3)B(l_1, l_2, l_3)$$
$$\approx \frac{(2\pi)^{3/2}}{(l_1 l_2 l_3)^{1/2}} B_{l_1 l_2 l_3} \sum_{m_1, m_2} e^{im_1(\phi_{l_1} - \phi_{l_3})}$$
$$\times e^{im_2(\phi_{l_2} - \phi_{l_3})} \begin{pmatrix} l_1 & l_2 & l_3 \\ m_1 & m_2 & -m_1 - m_2 \end{pmatrix} . \tag{20}$$

The triangle inequality of the Wigner-$3j$ symbol becomes a triangle equality relating the two-dimensional vectors. The implication is that the triplet (l_1, l_2, l_3) can be considered to contribute to the triangle configuration $l_1, l_2, l_3 = -l_1 + l_2$ where the multipole number is taken as the length of the vector.

2.3. Fisher Matrix

To quantify the amount of information contained about a parameter p_i in the bispectrum, we shall define the Fisher matrix F_{ij}. The Cramer-Rao inequality (Kendall & Stuart 1969) says that the variance of an unbiased estimator of p_i cannot be less than $(F^{-1})_{ii}$. In terms of the likelihood L of observing bispectrum elements $B_\alpha \equiv B_{l_1 l_2 l_3}$ (arranged as a data vector) given the true parameters p (called the fiducial model), the Fisher matrix is defined as

$$F_{ij} \equiv -\left\langle \frac{\partial^2 \ln L(B; p)}{\partial p_i \partial p_j}\right\rangle . \tag{21}$$

Under the approximation that the likelihood is Gaussian, this expression becomes

$$F_{ij} = \sum_{\alpha\alpha'} \frac{\partial B_\alpha}{\partial p_i} (C^{-1})_{\alpha\alpha'} \frac{\partial B_{\alpha'}}{\partial p_j} . \tag{22}$$

The covariance matrix between the α and α' bispectrum term is in general a complicated quantity to calculate (see Heavens 1998). However there are two simplifying assumptions that make this expression tractable. Firstly, since the CMB is expected to be nearly Gaussian, the dominant contribution to the covariance comes from the six-point function of the Gaussian field. This can be expressed in terms the power spectrum of all contributions to the field combined, i.e., the cosmic signal, detector noise, and residual foregrounds in the map,

$$C_l^{tot} = C_l + C_l^{noise} + C_l^{foreg} . \tag{23}$$

Secondly, assuming all-sky coverage[6] the power spectrum covariance is diagonal in l, m and the covariance then becomes (Luo 1994)

$$C_{\alpha\alpha'} \equiv \langle B_{l_1 l_2 l_3} B_{l'_1 l'_2 l'_3}\rangle$$
$$= C_{l_1}^{tot} C_{l_2}^{tot} C_{l_3}^{tot}[\delta^D(123) + \delta^D(231) + \delta^D(312)$$
$$+ \delta^D(213) + \delta^D(132) + \delta^D(321)] , \tag{24}$$

where

$$\delta^D(abc) = \delta^D_{l_1 l'_a} \delta^D_{l_2 l'_b} \delta^D_{l_3 l'_c} . \tag{25}$$

Here we have assumed that $l_1 \neq l_2$, $l_2 \neq l_3$, $l_1 \neq l_3$. The covariance increases by a factor of 2 when two ls are equal and by a factor of 6 when all three ls are equal.

Under these assumptions, the Fisher matrix reduces to

$$F_{ij} = \sum_{l_3 \geq l_2 \geq l_1} \sigma^{-2}_{l_1 l_2 l_3} \frac{\partial B_{l_1 l_2 l_3}}{\partial p_i} \frac{\partial B_{l_1 l_2 l_3}}{\partial p_j} , \tag{26}$$

where

$$\sigma^2_{l_1 l_2 l_3} = C_{l_1}^{tot} C_{l_2}^{tot} C_{l_3}^{tot}$$
$$\times (1 + \delta^D_{l_1 l_2} + \delta^D_{l_2 l_3} + \delta^D_{l_3 l_1} + 2\delta^D_{l_1 l_2}\delta^D_{l_2 l_3}) . \tag{27}$$

Note that the covariance between permutations of (l_1, l_2, l_3) restricts the sum to $l_3 \geq l_2 \geq l_1$.

Since the signal is expected to be small, in this paper we will be mainly concerned with the overall observability of

---

[6] Even satellite missions will not have all-sky coverage because of the need to remove galactic contamination. This will increase the covariance of the estimators but we neglect such subtleties here.

the bispectrum. Consider the most optimistic scenario where the form of the bispectrum is considered known and the only parameter of interest is its amplitude, i.e., $B_{l_1 l_2 l_3} = A B_{l_1 l_2 l_3}|_{\text{fid}}$ where the true value of $A = 1$. The Fisher matrix tells us that the variance of the measurements of A is no less than $\sigma^2(A) = (F^{-1})_{AA}$, or

$$\chi^2 \equiv \frac{1}{\sigma^2(A)} = \sum_{l_3 \geq l_2 \geq l_1} \frac{B_{l_1 l_2 l_3}^2}{\sigma_{l_1 l_2 l_3}^2} , \qquad (28)$$

which corresponds to the statistic introduced by Spergel & Goldberg (1999). We will often plot the contribution to χ^2 from a single l_3, summed over l_1, l_2 as $d\chi^2/dl_3$.

2.4. Detector Noise & Foregrounds

Detector noise will degrade the sensitivity of a given experiment to the bispectrum through equation (23). As pointed out by Knox (1995), detector noise in a given frequency channel v can be treated as an additional sky signal with a power spectrum

$$C_l^{\text{noise}}(v) = w^{-1}(v) e^{\theta^2(v) l(l+1)} , \qquad (29)$$

if the experimental beam is Gaussian with width $\theta(v)$ in radians (FWHM = $(8 \ln 2)^{1/2} \theta(v)$). Here the sensitivity measure $w^{-1}(v)$ is defined as the noise variance per pixel times the pixel area in steradians. Modern experiments have many frequency channels with independent pixel noise. In this case we inverse variance weight the noise so that

$$\frac{1}{C_l^{\text{noise}}} = \sum_v \frac{1}{C_l^{\text{noise}}(v)} , \qquad (30)$$

where the sum is over the different frequency channels.

We will use the *MAP* and *Planck* satellite specifications to illustrate the effects of detector noise (see Table 1). Note that this is somewhat optimistic since the multifrequency coverage of these experiments will have to be used to remove foreground contamination. Tegmark et al. (2000) have shown that given current expectations for foreground contributions, the increase in C_l^{tot} due to foreground removal is not expected to exceed $\sim 10\%$. Of course, the underlying premise that foregrounds add noise as a Gaussian random field is certainly incorrect at some level. It may well be that the bispectrum of the foregrounds is the limiting factor for observations of the cosmic bispectrum, a subject that lies beyond the scope of this paper. Figure 1 displays the total power as a sum of the cosmic spectrum and inverse-variance weighted noise spectrum for the *MAP* and *Planck* satellites.

2.5. Secondary Anisotropies

Secondary anisotropies in the CMB are those that are produced well after recombination at $z \sim 1000$. They generally fall into two broad classes: those arising from gravitational effects and those arising from Compton scattering.

The gravitational effects are due to gravitational redshift and lensing. The differential redshift effect from photons climbing in and out of a time-varying gravitational potential along the line of sight is called the integrated Sachs-Wolfe (ISW; Sachs & Wolfe 1967) effect while fluctuations are still linear, and the Rees-Sciama (Rees & Sciama 1968) effect for the second-order and nonlinear contributions. The ISW effect is important for low matter density universes, $\Omega_m < 1$, where the gravitational potentials decay at low redshift, and contributes anisotropies on and above the scale of the horizon at the time of decay (see Fig. 1 calculated from eq. [42]). The Rees-Sciama effect is small in adiabatic CDM models (Seljak 1996), and we will not consider it further here.

Gravitational lensing of the photons by the intervening large-scale structure both redistributes power in multipole space and enhances it because of power in the density perturbations. The most effective structures for lensing lie half way between the surface of recombination and the observer in comoving angular diameter distance. In the fiducial ΛCDM cosmology, this is at $z \sim 3.3$, but the growth of structure skews this to somewhat lower redshifts. In general, the efficiency of lensing is described by a broad bell-shaped
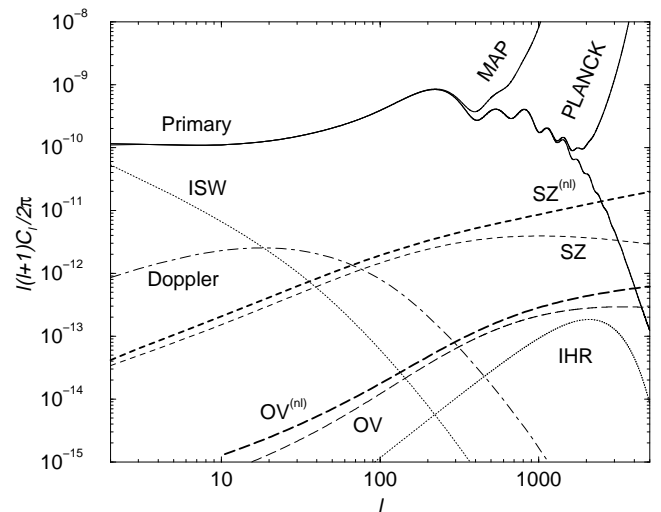
TABLE 1
DETECTOR NOISE SPECIFICATIONS

Experiment	v	FWHM	$10^6 \Delta T/T$
MAP	22	56	4.1
	30	41	5.7
	40	28	8.2
	60	21	11.0
	90	13	18.3
Planck	30	33	1.6
	44	23	2.4
	70	14	3.6
	100	10	4.3
	100	10.6	1.7
	143	7.4	2.0
	217	4.9	4.3
	353	4.5	14.4
	545	4.5	147
	857	4.5	6670

NOTE.—Specifications used for *MAP* and *Planck*. FWHM of the beams are in arcminutes. $w^{-1/2} = \Delta T \times \text{FWHM} \times \pi/10800$.

FIG. 1.—Power spectrum for the temperature anisotropies in the fiducial ΛCDM model with $\tau = 0.1 (\langle z_{\text{ri}} \rangle = 13) \Delta z = 0.1(1 + z_{\text{ri}})$ (see § 2.5 for details). The curve labeled "primary" actually includes the small ISW, Doppler, and lensing contributions. Note that the predictions for the SZ power spectrum are highly uncertain and frequency dependent. We have also shown the instrumental noise contribution of *MAP* and *Planck*, calculated using parameters in Table 1, which is important for signal-to-noise calculations.

function between the source and the observer. The curve labeled "primary" in Figure 1 includes the gravitational lensing effect on the power spectrum as calculated by the CMBFAST code (Seljak & Zaldarriaga 1996 and Zaldarriaga & Seljak 1997); lensing is responsible for the power-law tail of anisotropies for $l > 4000$ here.

Rescattering of the photons during the reionized epoch can both generate and erase anisotropies. The primary anisotropies are reduced as $\exp(-\tau)$ by scattering on small scales $l \gtrsim 50$. Density fluctuations can lead to optical depth variations and hence a patchy erasure of fluctuations. For the optically thin conditions considered here, this is a negligible effect.

The bulk flow of the electrons that scatter the CMB photons leads to a Doppler effect. Its effect on the power spectrum peaks around the horizon at the scattering event projected on the sky today (see Fig. 1). The contributions are strongly dependent on the optical depth in the reionized epoch; we take $\tau = 0.1$ as our fiducial model but explore optical depths up to $\tau = 0.5$. On scales smaller than the horizon at scattering, the contributions are mainly canceled as photons scatter against the crests and troughs of the perturbation. As a result, the Doppler effect is moderately sensitive to how rapidly the universe reionizes since contributions from a sharp surface of reionization do not cancel. Following current thinking that the universe reionized promptly (see Haiman & Knox 1999 for a review), we take $\Delta z = 0.1(1 + z_{\rm ri})$ in Figure 1.

The Sunyaev-Zel'dovich (SZ; Sunyaev & Zel'dovich 1980) effect arises from the inverse-Compton scattering of CMB photons by hot electrons along the line of sight. This effect has now been directly imaged toward massive galaxy clusters (e.g., Carlstrom, Joy, & Grego 1996), where temperature of the scattering medium can reach as high as 10 keV producing temperature changes in the CMB of order 1 mK. Here we are interested in the SZ effect produced by large-scale structure in the general intergalactic medium (IGM), where the exact calculation on its significance as a secondary anisotropy is not directly possible owing to the unknown distribution and clustering properties of baryonic gas and its temperature structure. Under certain simplifying, albeit largely untested assumptions detailed in § 3.5, its power spectrum is given in Figure 1 for both linear and nonlinear contributions. Given the untested assumptions, these spectra should be taken as provisional, even in their order of magnitude. Note that the SZ effect also bears a spectral signature that differs from the other effects. We have assumed observations in the Rayleigh-Jeans regime of the spectrum; an experiment such as *Planck*, with sensitivity beyond the peak of the spectrum, can separate out these contributions based on the spectral signature.

The Ostriker-Vishniac effect arises from the second-order modulation of the Doppler effect by density fluctuations (Ostriker & Vishniac 1986; Vishniac 1987). Its nonlinear analogue is the kinetic SZ effect from large-scale structure (Hu 2000); we denote it $\mathrm{OV}^{(\mathrm{nl})}$ here to avoid confusion with the thermal SZ effect. Because of its density weighting, the OV effect peaks at small scales: arcminutes for ΛCDM. For a fully ionized universe, contributions are broadly distributed in redshift so that the power spectra are moderately dependent on the optical depth τ, which we generally take to be 0.1.

Variations in the ionization fraction of the gas around the epoch of reionization can also modulate the Doppler effect

(Aghanim et al. 1996; Gruzinov & Hu 1998; Knox, Scoccimarro, & Dodelson 1998). This effect depends on the detailed physical processes occurring at reionization though it probably contributes substantially to the subarcminute-scale anisotropy. Because of the small scale of the effect and its unknown relationship to the density field and hence the other secondary effects, we do not consider its contribution to the power spectrum or bispectrum here.

In summary, for ΛCDM cosmologies with optical depths $\tau \sim 0.1$, the ISW contributions dominate at low l-values, the Doppler contributions cominate at intermediate l-values, and the SZ contributions dominate at small scales. Given the crudeness of the approximation for the SZ effect, one cannot rule out the possibility that OV contributions dominate at high values of l. The power spectra of these effects imply that the intrinsic contributions of the ISW, Doppler, and SZ effects are comparable but appear at different angular scales and arise from different redshifts. It is for this reason that we shall consider the bispectrum contributions from these effects in the following sections.

3. LENSING EFFECTS: DERIVATION

The general derivation of CMB bispectrum due to the coupling of lensing with secondary anisotropies, originally considered by Goldberg & Spergel (1999), is reviewed in § 3.1. It is applied to Doppler secondary anisotropies in § 3.2. For comparison, in §§ 3.3 and 3.4 we briefly revisit the coupling between gravitational lensing and ISW and SZ effects, respectively, studied by Goldberg & Spergel (1999).

3.1. *General Considerations*

Large-scale structure deflects CMB photons in transit from the last scattering surface. These structures also give rise to secondary anisotropies. The result is a correlation between the temperature fluctuations and deflection angles. This effect cannot be seen in the two-point function since gravitational lensing preserves surface brightness: deflections only alter the temperature field on the sky in the presence of intrinsic, primary, anisotropies in the unlensed distribution. The lowest order contribution thus comes from the three-point function or bispectrum.

In weak gravitational lensing, the deflection angle on the sky is given by the angular gradient of the lensing potential, which is itself a projection of the gravitational potential (see e.g., Kaiser 1992),

$$\Theta(\hat{m}) = -2 \int_0^{r_0} dr \, \frac{d_A(r_0 - r)}{d_A(r) d_A(r_0)} \, \Phi(r, \hat{m}r) \ . \tag{31}$$

This quantity is simply related to the more familiar convergence

$$\kappa(\hat{m}) = \frac{1}{2} \, \nabla^2 \Theta(\hat{m})$$

$$= - \int_0^{r_0} dr \, \frac{d_A(r) d_A(r_0 - r)}{d_A(r_0)} \, \nabla_\perp^2 \, \Phi(r, \hat{m}r) \ , \tag{32}$$

where note that the two-dimensional Laplacian operating on Φ is a spatial and not an angular Laplacian. The two terms κ and Θ contain superficial differences in their radial and wavenumber weights, which we shall see cancel in the appropriate Limber approximation. In particular, their

spherical harmonic moments are simply proportional,

$$\Theta_{lm} = -\frac{2}{l(l+1)}\,\kappa_{lm} = \int d\hat{n}\, Y_l^{m*}(\hat{n})\Theta(\hat{n})$$

$$= i^l \int \frac{d^3k}{2\pi^2}\, \delta(\mathbf{k}) Y_l^{m*}(\hat{\mathbf{k}}) I_\ell^{\mathrm{len}}(k)\,, \tag{33}$$

with

$$I_\ell^{\mathrm{len}}(k) = \int_0^{r_0} dr\, W^{\mathrm{len}}(k,r) j_l(kr)\,,$$

$$W^{\mathrm{len}}(k,r) = -3\Omega_m\left(\frac{H_0}{k}\right)^2 F(r)\frac{d_A(r_0-r)}{d_A(r)d_A(r_0)}\,. \tag{34}$$

Here we have used the Rayleigh expansion of a plane wave

$$e^{i\mathbf{k}\cdot\hat{n}r} = 4\pi \sum_{lm} i^l j_l(kr) Y_l^{m*}(\hat{\mathbf{k}}) Y_l^m(\hat{n}) \tag{35}$$

and the fact that $\nabla^2 Y_l^m = -l(l+1)Y_l^m$. In an open universe, one simply replaces the spherical Bessel functions with ultraspherical Bessel functions in expressions such as equation (34). Since this is the case, we present the derivation in flat space.

Since expressions of the type in equation (34) frequently occur in the following calculations, it is useful to note that it may be evaluated efficiently with a temporal version of the Limber approximation (Limber 1954) called the weak coupling approximation (Hu & White 1996):

$$I_l^X(k) \equiv \int_0^{r_0} dr\, W^X(k,r) j_l(kr)$$

$$\approx W^X(k,l/k) \int_0^\infty dr j_l(kr) \qquad \left(k\frac{W}{\dot{W}} \gg 1\right)$$

$$= W^X(k,l/k)\frac{\sqrt{\pi}}{2k}\frac{\Gamma[(l+1)/2]}{\Gamma[(l+2)/2]}\,, \tag{36}$$

and note that the ratio of gamma functions goes to $\sqrt{2/l}$ for $l \gg 1$. For the open universe generalization of this result, see Hu (2000). We employ this approximation for sufficiently high l-values (usually $l > 200$), where the difference between full integral and the approximation is sufficiently low ($<1\%$).

Assuming a relation between the multipole moments and I_l^X as in equation (33), we find that the cross-correlation power between X and Y then becomes

$$\langle a_{lm}^{X*} a_{lm}^Y \rangle = 4\pi \int \frac{dk}{k} \Delta^2(k) I_l^X(k) I_l^Y(k)$$

$$\approx \frac{2\pi^2}{l^3}\int_0^{r_0} dr d_A\, W^X\!\left(\frac{l}{d_A},r\right) W^Y\!\left(\frac{l}{d_A},r\right)\Delta^2\!\left(\frac{l}{d_A}\right), \tag{37}$$

where the approximation involves a change in variables $d_A = l/k$, and we have restored generality for open geometries where $r \neq d_A$ (see Hu 2000). Note that in the Limber approximation where d_A is interchangeable with l/k, the superficial difference in the weights for κ and Θ disappears.

The quantity of interest is the correlation between the deflection potential and secondary anisotropies

$$T^S(\hat{n}) = \sum a_{lm}^S Y_l^m(\hat{n})\,, \tag{38}$$

which becomes

$$\langle\Theta(\hat{n})T^S(\hat{m})\rangle = \sum_{lm} \langle\Theta_{lm}^* a_{lm}^S\rangle Y_l^{m*}(\hat{n}) Y_l^m(\hat{m})\,. \tag{39}$$

Again statistical isotropy guarantees that we may write the correlation as

$$\langle\Theta_{lm}^* a_{lm}^S\rangle \equiv b_l^S \equiv \frac{-2}{l(l+1)} C_l^{T\kappa}\,,$$

$$= 4\pi \int \frac{dk}{k} \Delta^2(k) I_l^S(k) I_l^{\mathrm{len}}(k)\,,$$

$$\approx \frac{2\pi^2}{l^3}\int_0^{r_0} dr\, d_A\, W^S\!\left(\frac{l}{d_A},r\right) W^{\mathrm{len}}\!\left(\frac{l}{d_A},r\right)\Delta^2\!\left(\frac{l}{d_A}\right), \tag{40}$$

where we have used equation (33) to relate the power spectrum b_l^S defined by Goldberg & Spergel (1999) and the κ-secondary cross power spectrum defined by Seljak & Zaldarriaga (1999). The last line represents the Limber approximation and we have assumed that the secondary anisotropies are linearly related to the density field projected along the line of sight,

$$a_{lm}^S = i^l \int \frac{d^3k}{2\pi^2} \delta(\mathbf{k}) I_l^S(k) Y_l^m(\hat{\mathbf{k}})\,,$$

$$I_l^S(k) = \int dr\, W^S(k,r) j_l(kr)\,. \tag{41}$$

Note that the power spectrum of the secondary effect is then given by

$$C_l^S = 4\pi \int \frac{dk}{k} \Delta^2(k) I_l^S(k) I_l^S(k)\,. \tag{42}$$

We will discuss explicit forms for W^S for specific secondary effects in the following sections.

Unfortunately, the secondary-lensing correlation is not directly observable. As pointed out by Goldberg & Spergel (1999), it does however have an effect on the bispectrum that is in principle observable. The lensed temperature fluctuation in a given direction is the sum of the primary fluctuation in a different direction plus the secondary anisotropy

$$T(\hat{n}) = T^P(\hat{n} + \nabla\Theta) + T^S(\hat{n}) \tag{43}$$

$$\approx \sum_{lm} [(a_{lm}^P + a_{lm}^S)Y_l^m(\hat{n}) + a_{lm}^P \nabla\Theta(\hat{n})\cdot\nabla Y_l^m(\hat{n})]\,,$$

or

$$a_{lm} = a_{lm}^P + a_{lm}^S + \sum_{l'm'} a_{l'm'}^P \int d\hat{n}\, Y_l^{m*}(\hat{n})\nabla\Theta(\hat{n})\cdot\nabla Y_{l'}^{m'}(\hat{n})\,. \tag{44}$$

Utilizing the definition of the bispectrum in equation (17), we obtain

$$B_{l_1 l_2 l_3} = \sum_{m_1 m_2 m_3} \begin{pmatrix} l_1 & l_2 & l_3 \\ m_1 & m_2 & m_3 \end{pmatrix}$$

$$\times \int d\hat{m}\, d\hat{n}\, Y_{l_2}^{m_2*}(\hat{m}) Y_{l_3}^{m_3*}(\hat{n}) C_{l_1}$$

$$\times \nabla Y_{l_1}^{m_1*}(\hat{m})\cdot\langle\nabla\Theta(\hat{m})T^S(\hat{n})\rangle + \mathrm{Perm.}\,, \tag{45}$$

where the five permutations are with respect to the ordering of (l_1, l_2, l_3).

Integrating by parts and simplifying further following Goldberg & Spergel (1999) leads to a bispectrum of the form

$$
B_{l_1 l_2 l_3} = - \begin{pmatrix} l_1 & l_2 & l_3 \\ 0 & 0 & 0 \end{pmatrix} \sqrt{\frac{(2l_1 + 1)(2l_2 + 1)(2l_3 + 1)}{4\pi}}
$$

$$
\times \left[\frac{l_2(l_2 + 1) - l_1(l_1 + 1) - l_3(l_3 + 1)}{2} C_{l_1} b_{l_3}^{S} + \text{Perm.} \right],
$$

$$(46)$$

where we have employed equation (A5) to perform the angular integration.

3.2. Doppler-Lensing Effect

The Doppler effect generates temperature fluctuations as

$$
T^{\text{dop}}(\hat{n}) = \int_0^{r_0} dr g(r)\hat{n} \cdot v(r, \hat{n}r) .
$$

$$(47)$$

With the help of equation (8),

$$
\hat{n} \cdot k = \sum_m \frac{4\pi}{3} k Y_1^m(\hat{n}) Y_1^{m*}(\hat{k}) ,
$$

$$(48)$$

and the Clebsh-Gordan coefficients for the addition of angular momenta with $l = 1$, we can write the multipole moments as

$$
a_{lm}^{\text{dop}} = -4\pi i^l \int \frac{d^3 k}{(2\pi)^3} \frac{\delta(k)}{k} Y_l^{m*}(\hat{k}) \int_0^{r_0} dr g \dot{G} j_l'(kr) .
$$

$$(49)$$

Through integration by parts, this expression can be brought into the standard form of equation (41) with

$$
W^{\text{dop}}(k, r) = \frac{1}{k^2} (\dot{g}\dot{G} + g\ddot{G}) ,
$$

$$(50)$$

through integration by parts.

Employing equation (40) for the lensing correlation, we obtain

$$
b_l^{\text{dop}} \approx -\frac{6\pi^2}{l^7} \Omega_m H_0^2 \int_0^{r_0} dr d_A^4 (\dot{g}\dot{G} + g\ddot{G})
$$

$$
\times F(r) \frac{d_A(r_0 - r)}{d_A(r_0)} \Delta^2(l/d_A) ,
$$

$$(51)$$

in the Limber approximation for $l \gtrsim 200$.

3.3. Double-Scattering Lensing Effect

As pointed out by Kaiser (1984), double-scattering effects must also be considered since the single-scattering contributions are canceled along the line of sight at short wavelengths. Equation (49) implies that the Doppler effect produces an isotropic temperature fluctuation in the photons which subsequently last-scatter into the line of sight,

$$
a_{00}^{\text{dop}}(k) Y_0^0 \equiv k^{-2} S^{\text{iso}}(k, r)\delta(k)
$$

$$
= \frac{\delta(k)}{k} \int_r^{r_0} dr' g \dot{G} j_1[k(r - r')] ,
$$

$$(52)$$

where g is to be interpreted as the visibility function for an observer at r, i.e., $g = \dot{\tau} \exp\left[-\tau(r') + \tau(r) \right]$. For scales that are much smaller than the width of the visibility function, i.e., approximately $k(r_0 - r) \gg 1$, one can take $g\dot{G}$ out of the

integral leaving

$$
S^{\text{iso}}(k, r) \approx \dot{\tau}\dot{G} .
$$

$$(53)$$

The contribution to the anisotropy today takes the standard form of equation (41)

$$
W^{\text{iso}}(k, r) = k^{-2} g(r) S^{\text{iso}}(k, r) .
$$

$$(54)$$

In the Limber limit, equation (40) can be simplified as

$$
b_l^{\text{iso}} \approx -\frac{6\pi^2}{l^7} \Omega_m H_0^2 \int_0^{r_0} dr d_A^4 (g\dot{\tau}\dot{G})
$$

$$
\times F(r) \frac{d_A(r_0 - r)}{d_A(r_0)} \Delta^2(l/d_A) ,
$$

$$(55)$$

again valid for $\ell \gtrsim 200$.

3.4. ISW Lensing Effect

The integrated Sachs-Wolfe effect (Sachs & Wolfe 1967) results from the late time decay of gravitational potential fluctuations. The resulting temperature fluctuations in the CMB can be written as

$$
T^{\text{ISW}}(\hat{n}) = -2 \int_0^{r_0} dr \dot{\Phi}(r, \hat{n}r) .
$$

$$(56)$$

Using the Poisson equation (eq. [7]), we can then bring the contributions into the standard form of equation (41)

$$
W^{\text{ISW}}(k) = -3\Omega_m \left(\frac{H_0}{k}\right)^2 \dot{F}(r) .
$$

$$(57)$$

The two-point function produced between gravitational lensing angular deflections and ISW effect can now be written as in the Limber limit as (Goldberg & Spergel 1999)[7]

$$
b_l^{\text{ISW}} \approx \frac{18\pi^2}{l^7} \Omega_m^2 H_0^4 \int_0^{r_0} dr \dot{F} F d_A^4 \frac{d_A(r_0 - r)}{d_A(r_0)} \Delta^2(l/d_A) .
$$

$$(58)$$

For calculational purposes, we employ numerical integration to l of 200 and use Limber approximated formulation thereafter.

3.5. SZ Lensing Effect

The SZ effect leads to an effective temperature fluctuation in the Rayleigh-Jeans part of the CMB given by the integrated pressure fluctuation along the line of sight:

$$
T^{\text{SZ}}(\hat{n}) = -2 \int_0^{r_0} dr g \left(\frac{k_B T_e}{m_e c^2}\right) \left[\delta_{\text{gas}} + \frac{\delta T_e}{T_e} \right](r, \hat{n}r) ,
$$

$$(59)$$

where k_B is the Boltzmann constant. Unfortunately, the clustering properties of the gas and its temperature structure is uncertain even with state of the art hydrodynamic simulations.

---

[7] Note that our Limber approximated correlation between lensing and ISW effect is factor 2 lower than eq. (14) of Goldberg & Spergel (1999); the same equation also contains an additional misprint with respect to weighing by their τ factors.
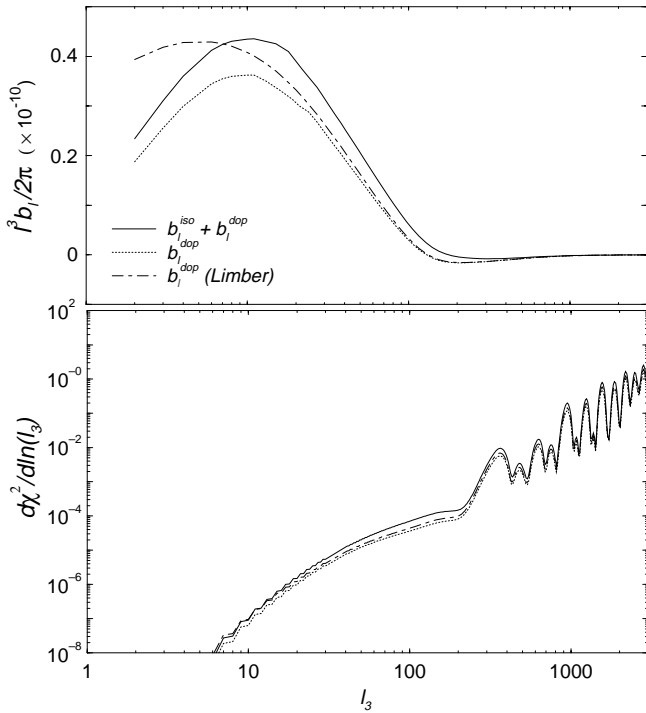
FIG. 2.—Doppler-lensing effect. Shown are the combined Doppler and double-scattering effects, (*solid line*), the Doppler effect (*dotted line*), and the Limber approximation to the Doppler effect (*dot-dashed* line). At sufficiently high l, the difference between these three treatments can be ignored for most practical purposes. *Top panel:* The correlation power spectrum. *Bottom panel:* Contribution to χ^2 per log interval in l_3.

To obtain an order of magnitude estimate of the effect, we follow Goldberg & Spergel (1999) in making several simplifying but largely untested assumptions. We assume that the gas is a biased tracer of the dark matter density $\delta_{gas} = b_{gas}\delta$ and that the IGM temperature distribution varies as $T_e(r) = a(r)T_{e0}$. Finally we ignore temperature fluctuations in the gas.

The effect can then be expressed as a weighted projection of the density field of the form in equation (41),

$$W^{SZ}(k) = -2A^{SZ}gaG , \tag{60}$$

with a normalization given by

$$A^{SZ} = b_{gas}\frac{k_B T_{e0}}{m_e c^2}$$

$$= 0.00783\left(\frac{b_{gas}}{4}\right)\left(\frac{T_{e0}}{1 \text{ keV}}\right). \tag{61}$$

For illustration purposes, we adopt $b_{gas} = 4$ and $T_{e0} = 1$ keV throughout.

The cross power between lensing and SZ can be written using equation (40):

$$b_l^{SZ} \approx \frac{12\pi^2}{l^5}\Omega_m H_0^2 A^{SZ} \int drG^2 d_A^2 g \frac{d_A(r_0 - r)}{d_A(r_0)}\Delta^2\left(\frac{l}{d_A}\right). \tag{62}$$

Since the SZ-lensing results in a correlation that peaks at $l \sim 100$ (see Goldberg & Spergel 1999), with no significant contribution at low l-values, the Limber approximation may be used to calculate the whole effect.

Both SZ effect and gravitational lensing angular deflection potentials will be enhanced by nonlinear fluctuations in the density field. To get a qualitative understanding of the effects, assume that the gas density and potential fluctuations continue to track the dark matter in the nonlinear regime. The nonlinear evolution of the dark matter density distribution has been well-studied with N-body simulations for adiabatic CDM cosmological models of interest here. We employ the scaling relation of Peacock & Dodds (1996) to obtain the nonlinear power spectrum today (see Fig. 4) as well as its evolution in time. In Figure 1, the curve labeled "SZ(nl)" is the power spectrum formed by the SZ effect using the nonlinear matter density power spectrum. The nonlinear effects generally increases the power due to SZ temperature fluctuations by a factor of 3 to 4 when l is in the interested range of 1000 to 5000.

With the introduction of the nonlinear power spectrum, we can write the cross-correlation between lensing and SZ as

$$b_l^{SZ(nl)} \approx \frac{12\pi^2}{l^5}\Omega_m H_0^2 A^{SZ}$$

$$\times \int dr d_A^2 g \frac{d_A(r_0 - r)}{d_A(r_0)}\Delta^{2(nl)}\left(\frac{l}{d_A}, r\right). \tag{63}$$

Since the nonlinear power spectrum no longer grows as G^2, it must be evaluated along the line of sight at the corresponding look-back time.

4. LENSING EFFECTS: RESULTS

4.1. *Doppler-Lensing Bispectrum*

The contribution to the bispectrum from the coupling of lensing to the Doppler effect is encapsulated in the power spectrum of the correlation b_l^{dop} (see eq. [51]). Figure 2 (*top*) shows its value for the Doppler effect in our fiducial ΛCDM $\tau = 0.1$ cosmology assuming cosmic variance only $C_l^{tot} = C_l$ (see eq. [23]). The zero crossing at $l \sim 100$ is due to the competition between contributions on the reionization surface and those from the intermediate redshifts. Likewise the Limber approximation to the integral also becomes excellent beyond $l = 200$. The inclusion of double-scattering contributions to the Doppler effect only makes a minor difference for $\tau \sim 0.1$.

We also show the contribution to the overall signal to noise squared (χ^2) per logarithmic interval in l_3 in Figure 2 (*bottom*). The minor differences in the χ^2 contributions at high l_3 between the Limber-approximated and Doppler-only spectra from the full calculation are primarily due to the differences of the b_l term at low l-values. Low l-values in b_l contribute to high l_3-values in χ^2 since the latter is a sum over $l_1 \leq l_2 \leq l_3$. The structure in the χ^2 plot and the rapid increase of its values around $l \sim 1000$ arises in large part from the structure of the primary C_l itself, which determines the Gaussian noise per mode.

Since the signal is dominated by the smallest angular scales available in the measurements, it is important to include the experimental beam and instrumental noise contributions. In Figure 3, we show the signal-to-noise ratio per mode of l_3 assuming *MAP* and *Planck* noise (see Table 1). Here we also show the affect of varying the optical depths from 0.1 to 0.5. Note that because reionization decreases the power spectrum of the anisotropies as $e^{-2\tau}$,

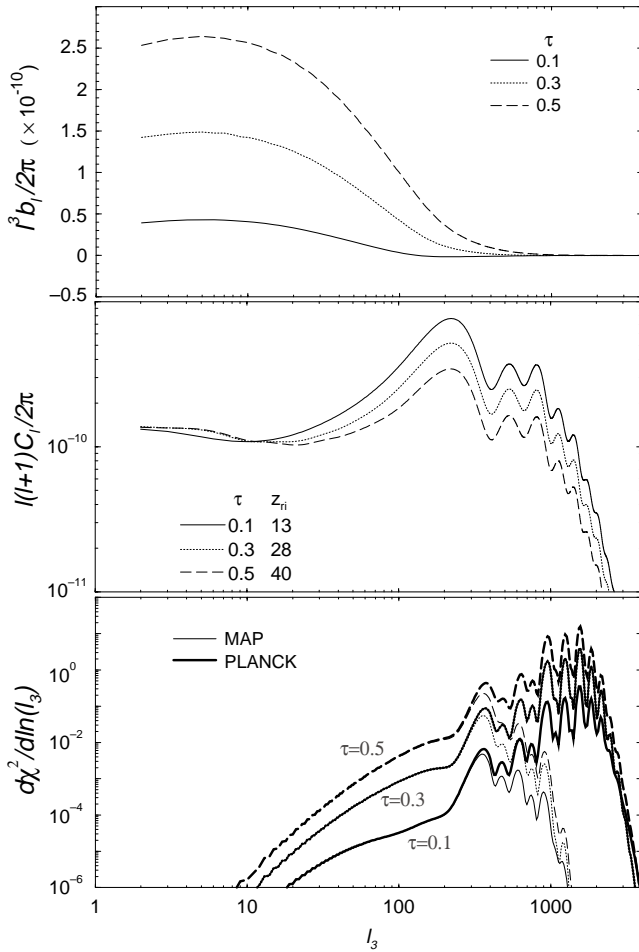FIG. 3.—Dependence of the Doppler-lensing effect on the ionization optical depth for τ of 0.1, 0.3 and 0.5 with $\Delta z = 0.1(1 + z_{ri})$. *Top panel:* The b_l term for the Doppler-lensing effect. *Middle panel:* CMB power spectrum used in the noise calculation. *Lower panel:* The contribution to χ^2 per log interval in l_3 with *MAP* and *Planck* detector noise included.

the Gaussian noise in the bispectrum is also decreased with increasing optical depth. We have assumed a reionization width of $\Delta z = 0.1(1 + z_{ri})$ here, but the lensing correlation is not sensitive to this parameter. The lensing efficiency is a
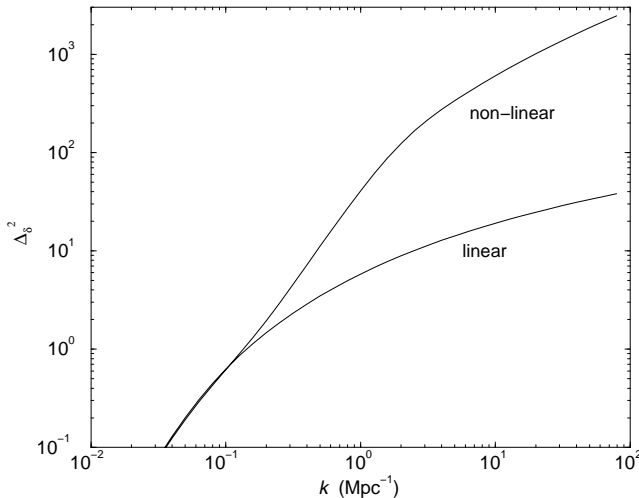
FIG. 4.—Linear and nonlinear density power spectra for the dark matter under the Peacock & Dodds (1996) scaling approximation for our fiducial ΛCDM cosmological model evaluated at the present.

broad bell-shaped function in angular diameter distance and does not correlate well with contributions localized near the distant surface of reionization.

As shown in Figure 3, the bispectrum mode contribution to χ^2 for any l_3 due to coupling between reionized Doppler effect and gravitational lensing angular deflections is generally less than 10^{-2}, unless the optical depth to reionization is greater than what is currently inferred from the observed power spectrum of anisotropies ($\tau < 0.5$; Griffiths, Barbosa, & Liddle 1999; see Haiman & Knox 1999 for a recent review). Adding all the l_3 mode contributions, the total χ^2-value is generally at a level below where one can expect its detection in the upcoming satellite data for reasonable optical depths ($\tau \lesssim 0.3$).

4.2. *Comparison of Lensing Effects*

In Figure 5 we compare the relative contribution to the CMB bispectrum from all the effects calculated. Both ISW and Doppler effects contribute at low l-values to the correlation $l^3 b_l/2\pi$, while SZ effect to $l \sim 100$. The Doppler-lensing coupling is suppressed by a factor of ~ 8 when compared to ISW-lensing coupling, which is in large part
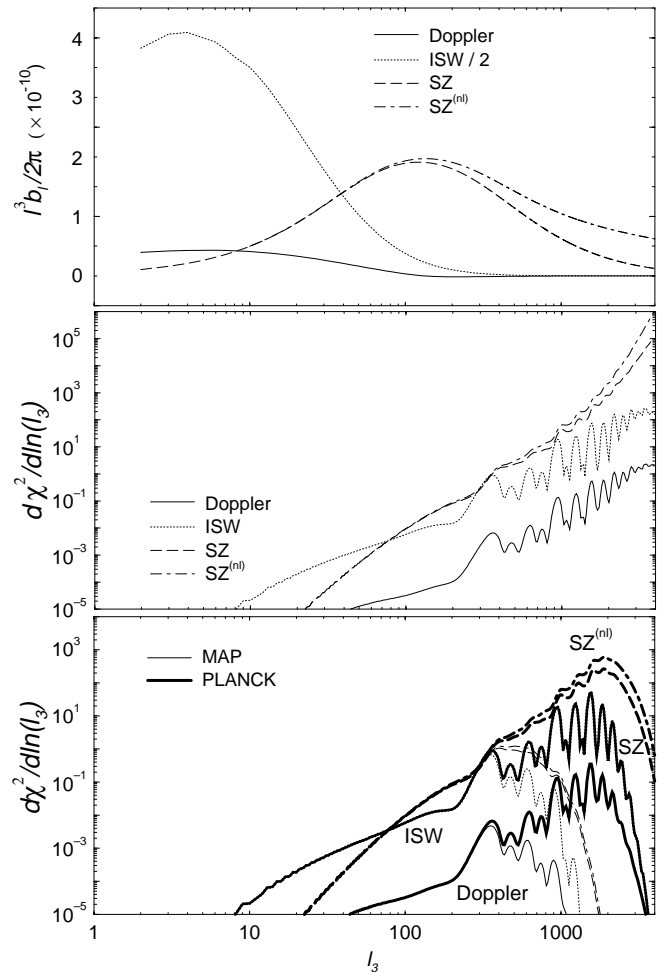

FIG. 5.—Comparison of various lensing effects for our fiducial ΛCDM model and with $\tau = 0.1$ and $\Delta z = 0.1(1 + z_{ri})$. *Top panel:*— The power spectrum of the correlation. *Middle panel:* Contributions to χ^2 per log interval in l_3, assuming cosmic variance only. *Lower panel—:* The same adding in detector noise for *MAP* and *Planck*.
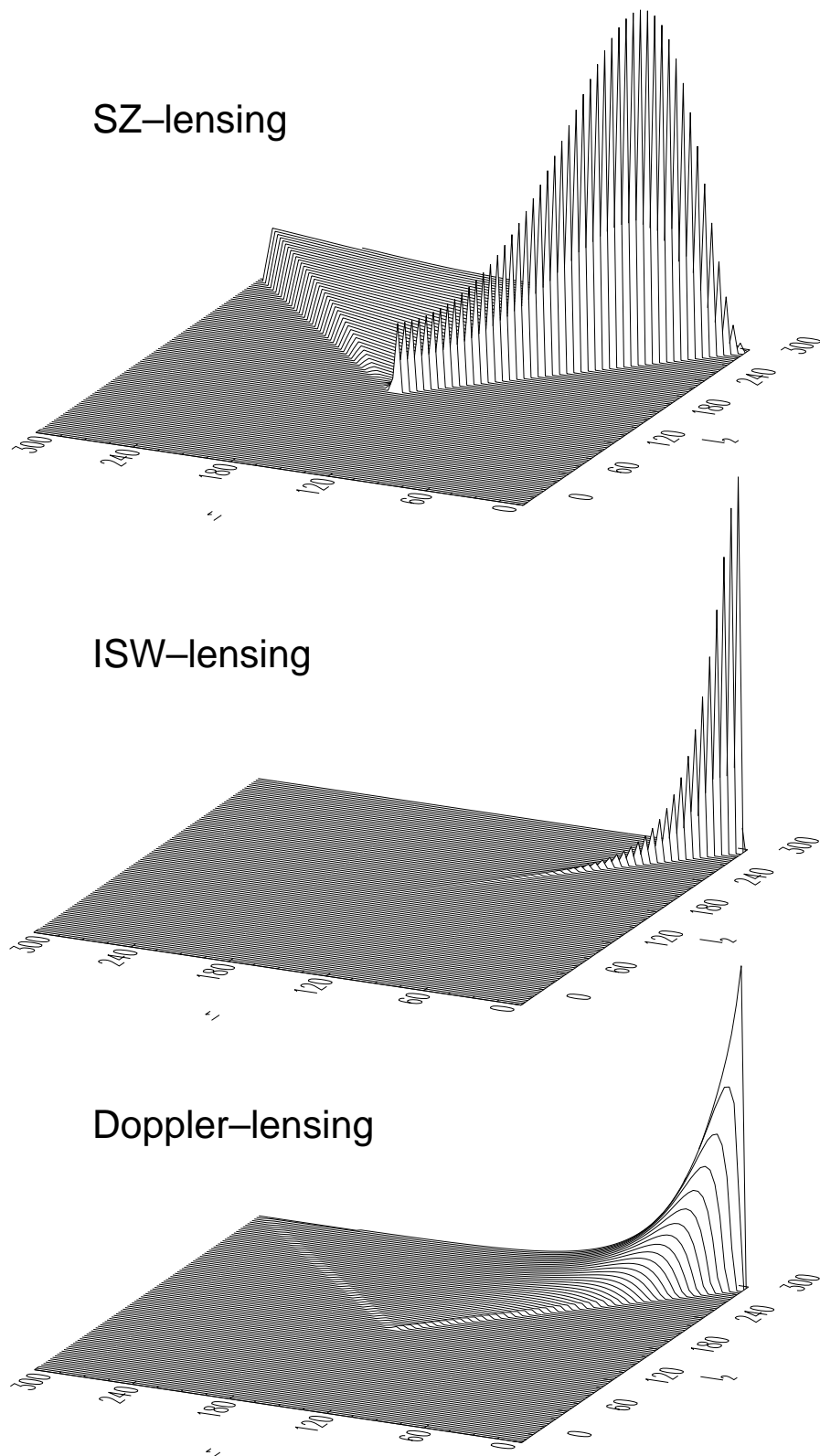
FIG. 6.—Configuration dependence of the secondary-lensing signal. Plotted is the contributions to χ^2 of from single mode $l_3 = 300$ as a function of l_2 and l_1. The configuration shapes are determined by both the power spectra of the cross-correlation (b_l terms; see Fig. 5) and the CMB power spectrum. The spiky behavior in these plots is an artifact of the plotting near the sharp crest introduced by the Wigner-3j symbol (see Fig. 10).

due to the inefficiency with which high-redshift structures lens the CMB. As shown, the SZ-lensing coupling and ISW-lensing coupling dominate the Doppler-lensing effect for optical depths $\tau \lesssim 0.5$. The nonlinear growth of fluctuations increases the SZ-lensing cross-correlation when $l > 100$ when compared to pure linear effects with a modest enhancement factor of ~ 5 at $l \sim 5000$. Such an enhancement in the SZ-lensing cross-correlation power spectrum is
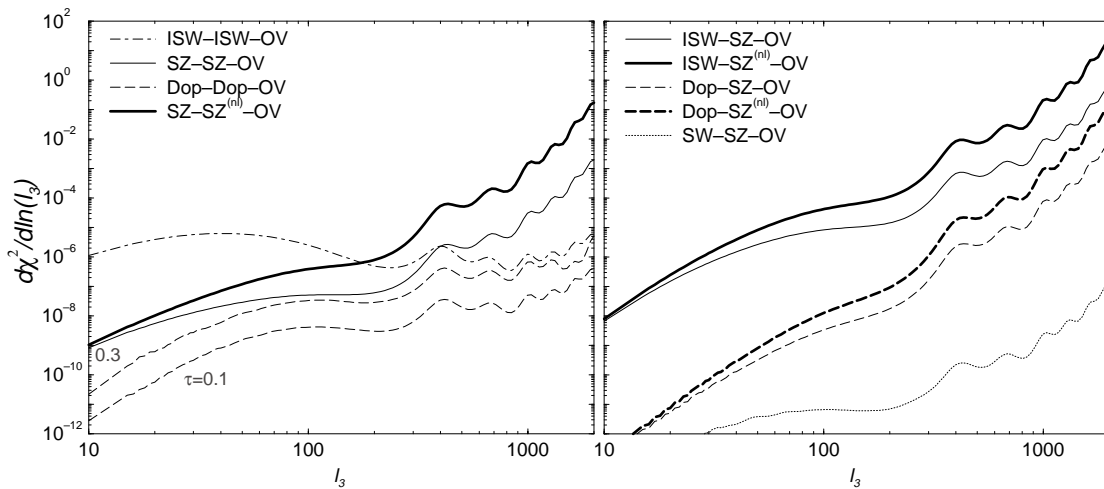
Fig. 7.—Contribution to χ^2 per log interval in l_3 for the OV coupling effects for the fiducial ΛCDM model with $\tau = 0.1$, $\Delta z = 0.1(1 + z_{ri})$ and no instrumental noise. *Left panel:* Coupling with two secondary effects of the same kind. *Right panel:* Hybrid effects involving secondaries of different kind. Other than Doppler-Doppler-OV and Doppler-SZ-OV couplings, the secondary-secondary-OV bispectra are only mildly sensitive to the reionized optical depth and width.

consistent with increases in both SZ and lensing individual power spectra due to nonlinear effects.

If untested assumptions on the SZ thermal effect were found to be false and the SZ contribution to be lower than currently presumed, than most of the contribution, at least in a low-Ω_m flat cosmological model, would come from coupling between gravitational lensing and the ISW effect. However, even if this turns out to be the case, one may be able to use the spectral signature of the SZ effect to separate its contribution. If SZ-lensing coupling is clearly detected, it would also support the current notion that most of baryons are present in the IGM as form of a gas at temperature of ~ 1 keV. As suggested by Goldberg & Spergel (1999), this would certainly solve the "missing baryons" problem (Cen & Ostriker 1999). In the meantime, improvements of our knowledge of the physical nature of the baryonic gas is clearly needed and can come from both observations as well as numerical simulations (e.g., da Silva et al. 1999).

Another obstacle for the unambiguous detection of the SZ, ISW and Doppler lensing effects is the ability to distinguish their bispectrum contribution from those of other physical mechanisms. The χ^2 statistic of Goldberg & Spergel (1999) lumps all the information on each effect into one number and makes such an assessment difficult. Once all the effects are known the question of separability can be addressed with the Fisher matrix techniques of § 2.3. In the meantime, it is useful to ask what combination of (l_1, l_2, l_3) is most of the signal coming from, i.e., what triangle configurations in the bispectrum dominate. In Figure 6 as an example, we show the general behavior of individual mode contribution to our signal-to-noise statistic χ^2 as a function of l_1 and l_2. Here we have taken $l_3 = 300$, which is representative of the their behavior in the l_3 range of interest. Since $B^2(l_1, l_2, l_3)$ is zero when $l_1 + l_2 + l_3$ is odd, we have omitted these values for plotting purposes.

The configuration dependences results from a combination of the secondary-lensing cross-correlation power spectra and the CMB power spectrum. They are modulated by the behavior of the Wigner-3j symbol and variations in the noise term from the CMB power spectra. As shown in Figure 10, the Wigner-3j symbol also peaks at the lowest l_1 that satisfies the triangle rule $l_1 = l_3 - l_2$. The CMB power spectrum noise introduces features associated with the acoustic peaks at $l \gtrsim 200$ (see Figs. 3 and 5).

The SZ-lensing bispectrum gets most of its contribution when $l_1 \sim l_3 - l_2$ with l_1 taking values in the intermediate l-range of few hundreds where the cross-power peaks. This behavior also suggest why the SZ$^{(nl)}$-lensing bispectrum is not strongly enhanced even at high l_3-values by nonlinear effects, as most of the contributions come from intermediate $b_l^{SZ(nl)}$ values, where nonlinear enhancement is negligible.

For ISW-lensing, the cross-correlation term peaks toward low l- values, and thus, its configuration dependence is such that the contributions to bispectrum peaks when $l_1 \sim l_3 - l_2$ with l_1 in the range of few tens. This behavior continues out to high l_3-values.

The Doppler-lensing configuration also shows a similar behavior but with contributions from somewhat smaller $l_1 \lesssim l_3 - l_2$, with l_1 again taking values close to the peak in the cross-correlation power spectrum. These subtle differences in configuration may assist in isolating and identifying the various contributions to the bispectrum once it is observed.

5. OSTRIKER-VISHNIAC COUPLING: DERIVATION

We consider the generation of CMB bispectra through coupling between the second order reionized Ostriker-Vishniac (OV) effect and two other linear sources of anisotropies. Since the OV effect is itself a secondary anisotropy source, we shall see that it only couples to other secondary anisotropy sources. First, we present a general derivation of the coupling between OV effect and secondary effects and in § 5.1 and then turn to specific secondary effects such as the ISW, SZ and reionized Doppler effect.

5.1. *General Considerations*

The OV effect arises from the modulation of the Doppler effect by density fluctuations, which affect the probability of scattering (Ostriker & Vishniac 1986; Vishniac 1987). The

OV temperature fluctuations can be written as

$$T^{OV}(\hat{n}) = \int dr g(r) \boldsymbol{n} \cdot \boldsymbol{v}(r, \hat{n}r)\delta(r, \hat{n}r)$$

$$= -i \int dr g \dot{G} G \int \frac{d^3k}{(2\pi)^3} \int \frac{d^3k'}{(2\pi)^3}$$

$$\times \delta(\boldsymbol{k} - \boldsymbol{k}')\delta(\boldsymbol{k}')e^{i\boldsymbol{k}\cdot\hat{n}r}[\hat{n} \cdot \boldsymbol{D}(\boldsymbol{k}, \boldsymbol{k}')] , \quad (64)$$

where

$$\boldsymbol{D}(\boldsymbol{k}, \boldsymbol{k}') = \frac{1}{2}\left[\frac{\boldsymbol{k} - \boldsymbol{k}'}{|\boldsymbol{k} - \boldsymbol{k}'|^2} + \frac{\boldsymbol{k}'}{k'^2}\right] , \quad (65)$$

is the projection vector that couples the density and velocity perturbations.

We can now expand out the temperature perturbation, T^{OV}, into spherical harmonics:

$$a_{lm}^{OV*} = i \int d\hat{n} \int dr(g\dot{G}G) \int \frac{d^3k_1}{(2\pi)^3} \int \frac{d^3k_2}{(2\pi)^3} \delta^*(\boldsymbol{k}_1)\delta^*(\boldsymbol{k}_2)$$

$$\times e^{-i(\boldsymbol{k}_1+\boldsymbol{k}_2)\cdot\hat{n}r}[\hat{n} \cdot \boldsymbol{D}(\boldsymbol{k}_1, \boldsymbol{k}_2)]Y_l^m(\hat{n}) , \quad (66)$$

where we have symmetrized by using $\boldsymbol{k}_1$ and $\boldsymbol{k}_2$ to represent $\boldsymbol{k}$ and $\boldsymbol{k} - \boldsymbol{k}'$, respectively. Now the dot product between $\hat{n}$ and the projection vector is

$$\hat{n} \cdot \boldsymbol{D}(\boldsymbol{k}_1, \boldsymbol{k}_2) = \frac{1}{2}\left(\frac{\hat{n} \cdot \boldsymbol{k}_1}{k_1^2} + \frac{\hat{n} \cdot \boldsymbol{k}_2}{k_2^2}\right) , \quad (67)$$

with

$$\hat{n} \cdot \boldsymbol{k} = \sum_{m'} \frac{4\pi}{3} k Y_1^{m'}(\hat{n})Y^{m'*}_1(\hat{k}) . \quad (68)$$

Since the dot product is symmetric, we consider only one term here, and multiply the result by 2. By using the Rayleigh expansion (eq. [35]), we can rewrite the multipole moments as

$$a_{lm}^{OV*} = i \frac{(4\pi)^3}{3} \int dr \int \frac{d^3k_1}{(2\pi)^3} \int \frac{d^3k_2}{(2\pi)^3} \sum_{l_1m_1} \sum_{l_2m_2} \sum_{m'}$$

$$\times (-i)^{l_1+l_2}(g\dot{G}G)\frac{j_{l_1}(k_1 r)}{k_1}j_{l_2}(k_2 r)\delta^*(\boldsymbol{k}_1)\delta^*(\boldsymbol{k}_2)$$

$$\times Y_{l_1}^{m_1*}(\hat{k}_1)Y^{m'*}_1(\hat{k}_1)Y_{l_2}^{m_2*}(\hat{k}_2)$$

$$\times \int d\hat{n} Y_l^m(\hat{n})Y_{l_1}^{m_1}(\hat{n})Y_{l_2}^{m_2}(\hat{n})Y_1^{m'}(\hat{n}) . \quad (69)$$

The power spectrum of the OV effect may be calculated from this expression. Since the end expression is cumbersome, we revert to the expressions of Hu (2000) in calculating the OV power spectrum shown in Figure 1.

To leading order in $\Delta^2(k)$, bispectrum contributions involve one OV term and two linear sources of anisotropies. Recall that a general linear effect can be expressed as a weighted projection of the density field (see §3.1)

$$a_{lm}^S = i^l \int \frac{d^3k}{2\pi^2} \delta(\boldsymbol{k})I_l^S(k)Y_l^m(\hat{k}) ,$$

$$I_l^S(k) = \int dr W^S(k, r)j_l(kr) . \quad (70)$$

After some straightforward but tedious algebra, we can write

$$a_{l_1m_1}^S a_{l_2m_2}^S a_{l_3m_3}^{OV*} = (4\pi)^2 \int \frac{dk_1}{k_1} \int \frac{dk_2}{k_2} \Delta^2(k_1)\Delta^2(k_2)$$

$$\times I_{l_1}^S(k_1)I_{l_2}^S(k_2)[I_{l_1,l_2}^{OV}(k_1, k_2)$$

$$+ I_{l_1,l_2}^{OV}(k_2, k_1)]$$

$$\times \int d\hat{n} Y_{l_3}^{m_3}(\hat{n})Y_{l_2}^{m_2*}(\hat{n})Y_{l_1}^{m_1*}(\hat{n}) , \quad (71)$$

where

$$I_{l_1,l_2}^{OV}(k_1, k_2) = \int dr W^{OV}j_{l_2}(k_2 r)j'_{l_1}(k_1 r) ,$$

$$W^{OV}(k_1, r) = -\frac{1}{k_1} g\dot{G}G . \quad (72)$$

In simplifying the integrals involving spherical harmonics, we have made use of the properties of Clebsch-Gordon coefficients, in particular, those involving $l = 1$.

In order to construct the bispectrum, note that

$$\langle a_{l_1m_1}^S a_{l_2m_2}^S a_{l_3m_3}^{OV}\rangle = (-1)^{l_3}\langle a_{l_1m_1}^S a_{l_2m_2}^S a_{l_3-m_3}^{OV*}\rangle . \quad (73)$$

Under the assumption that "S" denotes the sum of all the sources so that the two contributions are indistinguishable, the bispectrum becomes

$$B_{l_1l_2l_3} = \sum_{m_1m_2m_3}\begin{pmatrix} l_1 & l_2 & l_3 \\ m_1 & m_2 & m_3 \end{pmatrix}(\langle a_{l_1m_1}^S a_{l_2m_2}^S a_{l_3m_3}^{OV}\rangle$$

$$+ \langle a_{l_2m_2}^S a_{l_3m_3}^S a_{l_1m_1}^{OV}\rangle + \langle a_{l_3m_3}^S a_{l_1m_1}^S a_{l_2m_2}^{OV}\rangle)$$

$$= \sqrt{\frac{(2l_1 + 1)(2l_2 + 1)(2l_3 + 1)}{4\pi}}\begin{pmatrix} l_1 & l_2 & l_3 \\ 0 & 0 & 0 \end{pmatrix}$$

$$\times [b_{l_1,l_2}^{S-S} + \text{Perm.}] . \quad (74)$$

where we have used equations (A5), (A2), and (A6). Here

$$b_{l_1,l_2}^{S-S} = (4\pi)^2 \int \frac{dk_1}{k_1} \int \frac{dk_2}{k_2} \Delta^2(k_1)\Delta^2(k_2)$$

$$\times I_{l_1,l_2}^{OV}(k_1, k_2)I_{l_1}^S(k_1)I_{l_2}^S(k_2) . \quad (75)$$

Note that we have rewritten the $k_1 \to k_2$ term in equation (71) as an $l_1 \to l_2$ interchange so that in equation (74) "Perm." means a sum over the remaining 5 permutations of (l_1, l_2, l_3) as usual. In the following sections, we evaluate this expression with

$$I_l^S(k) = I_l^{ISW}(k) + I_l^{SZ}(k) + I_l^{dop}(k) + I_l^{SW}(k) . \quad (76)$$

The last term is the Sachs-Wolfe effect, which we explicitly consider to show that the OV effect mainly couples with secondary not primary anisotropies. We drop the double-scattering effect of § 3.3, as it is a small contribution for small optical depths. Note that expanding I^S in equation (75) produces many cross-terms, which we will call hybrid effects.

In general, equation (75) involves five integrations, three over radial distances and two over wavenumbers. As in the

lensing bispectrum calculation, these integrals can be simplified using the Limber approximation for sufficiently large (l_1, l_2). Here we employ a version based on the completeness relation of spherical Bessel functions:

$$\int dk\,k^2 F(k) j_l(kr) j_l(kr') \approx \frac{\pi}{2} d_A^{-2} \delta^D(r - r') F(k)|_{k=(l/d_A)}\,, \quad (77)$$

where the assumption is that $F(k)$ is a slowly varying function. Applying this to the integral over k_2 yields

$$
\begin{aligned}
b_{l_1,l_2}^{S-S} \approx (4\pi)^2\,\frac{\pi}{2} \int dr \int dr_1 \int \frac{dk_1}{k_1}\,\frac{1}{k_2^3}\,\Delta^2(k_1)\Delta^2(k_2) \\
\times\, W^S(k_1, r_1)\,\frac{W^S(k_2, r)W^{OV}(k_1, r)}{d_A^2}\bigg|_{k_2 = (l_2/d_A)} \\
\times\, j'_{l_1}(k_1 r) j_{l_1}(k_1 r_1)\,.
\end{aligned} \quad (78)
$$

Integrating by parts and assuming negligible boundary terms yields

$$
\begin{aligned}
b_{l_1,l_2}^{S-S} \approx -4\pi^4 \int dr\,\frac{1}{k_1^4 k_2^3}\,\Delta^2(k_1)\Delta^2(k_2)\,\frac{W^S(k_1, r)}{d_A^2} \\
\times\,\frac{d}{dr}\left[\frac{W^{OV}(k_1, r)W^S(k_2, r)}{d_A^2}\right]\bigg|_{k_1 = (l_1/d_A), k_2 = (l_2/d_A)} \\
\approx 4\pi^4 \int dr\,\frac{1}{k_1^4 k_2^3}\,\Delta^2(k_1)\Delta^2(k_2)\,\frac{d}{dr}\left[\frac{W^S(k_1, r)}{d_A^2}\right] \\
\times\,\frac{W^{OV}(k_1, r)W^S(k_2, r)}{d_A^2}\bigg|_{k_1 = (l_1/d_A), k_2 = (l_2/d_A)}\,.
\end{aligned} \quad (79)
$$

This Limber approximation reduces the dimension of the integrals from 5 to 1. Note that where the Limber approximation applies only equal time correlations contribute. On small angular scales, then, only secondary, not primary, anisotropies couple to the OV effect in the bispectrum.

5.2. ISW-ISW-OV coupling

Recall that from §3.4, the weight function for the ISW effect is

$$W^{ISW}(k, r) = -\frac{3\Omega_m H_0^2}{k^2}\,\dot{F}\,. \quad (80)$$

Substituting this weight function into equation (79) leads to

$$
\begin{aligned}
b_{l_1,l_2}^{ISW-ISW} = -\frac{36\pi^4}{l_1^7 l_2^5}\,\Omega_m^2 H_0^4 \int_0^{r_0} dr\,\Delta^2\!\left(\frac{l_1}{d_A}\right)\Delta^2\!\left(\frac{l_2}{d_A}\right) \\
\times\, d_A^{10}\,g\dot{G}G\left(\frac{d}{dr}\,\frac{\dot{F}}{d_A^2}\right)\dot{F}\,.
\end{aligned} \quad (81)
$$

We employ this Limber approximation in our calculation of the ISW-ISW-OV bispectrum effect.

5.3. SZ-SZ-OV

In a similar manner, we can calculate the SZ-SZ-OV effect following the discussion in § 3.5 where the weight function is given as

$$W^{SZ}(k, r) = -2A^{SZ}agG\,, \quad (82)$$

and is independent of the wave vector $\boldsymbol{k}$. Now the Limber approximated bispectrum term, used in the calculations

presented here, is

$$
\begin{aligned}
b_{l_1,l_2}^{SZ-SZ} = -\frac{16\pi^4}{l_1^5 l_2^3}\,(A^{SZ})^2 \int_0^{r_0} dr\,\Delta^2\!\left(\frac{l_1}{d_A}\right)\Delta^2\!\left(\frac{l_2}{d_A}\right) \\
\times\, ag^2 G^2 \dot{G} d_A^6\left(\frac{d}{dr}\,\frac{agG}{d_A^2}\right).
\end{aligned} \quad (83)
$$

Similar to our calculation on the enhancement of SZ-lensing bispectrum due to nonlinear growth of density fluctuations, we also consider the effect of nonlinearities on the SZ-SZ-OV bispectrum. As shown in Figure 1, nonlinearities enhance both SZ and OV effects and at high l, the OV effect involves the large-scale velocity field and small-scale density field in the nonlinear regime (Hu 2000). For the bispectrum coupling, therefore, we replace only one of the power spectrum terms with the nonlinear relation,

$$
\begin{aligned}
b_{l_1,l_2}^{SZ(nl)-SZ} = -\frac{16\pi^4}{l_1^5 l_2^3}\,(A^{SZ})^2 \int_0^{r_0} dr\,\Delta^2\!\left(\frac{l_1}{r}\right)\Delta^{2(nl)}\!\left(\frac{l_2}{r}, r\right) \\
\times\, d_A^6\left(\frac{d}{dr}\,\frac{agG}{d_A^2}\right)ag^2\dot{G}\,.
\end{aligned} \quad (84)
$$

As before, with SZ-lensing nonlinear cross-correlation, the SZ-SZ$^{(nl)}$-OV coupling is calculated with the nonlinear density power spectrum evaluated along the line of sight at the corresponding look-back time.

5.4. Doppler-Doppler-OV

The reionized Doppler effect was discussed in detail in § 3.2 and has a weight function

$$W^{dop}(k, r) = \frac{1}{k^2}\,(\dot{g}\dot{G} + g\ddot{G})\,. \quad (85)$$

Unlike ISW-ISW-OV and SZ-SZ-OV, where the Limber approximation is sufficiently accurate for our purposes, explicit integration over wavenumber is necessary here. The Limber approximation breaks down in the large-angle regime and hence affects the coupling between the velocity field in the OV effect and the Doppler effect. On the other hand, the density field in the OV effect is dominated by small-scale fluctuations where the Limber approximation is excellent. This implies that we may use equation (78) in calculating the Doppler-Doppler-OV effect:

$$
\begin{aligned}
b_{l_1,l_2}^{dop-dop} = -\frac{8\pi^3}{l_2^5} \int \frac{dk}{k^2}\,\Delta^2(k) \int dr\,\Delta^2\!\left(\frac{l_2}{d_A}\right) \\
\times\, g\dot{G}G d_A^3(\ddot{G}g + \dot{G}\dot{g}) j'_{l_1}(kr) I_{l_1}^{dop}(k)\,.
\end{aligned} \quad (86)
$$

The integrals above include a derivative of the Bessel function and is numerically difficult to evaluate. As in equation (79), one can integrate by parts to obtain a more tractable form. We considered both these approaches and the resulting bispectra agree at a level of 10%, with most of the difference resulting from the numerical computation of the coupling term involving the derivative of the Bessel function. This agreement also suggests that the evaluation at $k = l/d_A$ in the Limber approximation can be performed after all the integration by parts are complete as is assumed in equation (79).

5.5. ISW-SZ-OV

In addition to coupling between OV effect and secondary anisotropies of similar kind, we also consider hybrid coup-

lings. The hybrids that contribute the most involve a large-scale effect such as the ISW effect to couple with the velocity field in the OV effect, and a small-scale effect such as the SZ effect to couple with the density field in the OV effect,

$$
b_{l_1,l_2}^{\mathrm{ISW}-\mathrm{SZ}} = -\frac{24\pi^4}{l_1^7 l_2^3}\, \Omega_m H_0^2\, A^{\mathrm{SZ}} \int dr \Delta^2\!\left(\frac{l_1}{r}\right)\Delta^2\!\left(\frac{l_2}{r}\right)
$$

$$
\times\, G^2 g^2 a \dot{G} d_A^8\!\left(\frac{d}{dr}\frac{\dot{F}}{d_A^2}\right). \tag{87}
$$

To estimate the effects of nonlinearities, we take the approximations introduced for the SZ-SZ$^{(\mathrm{nl})}$-OV above and find

$$
b_{l_1,l_2}^{\mathrm{ISW}-\mathrm{SZ(nl)}} = -\frac{24\pi^4}{l_1^7 l_2^3}\, \Omega_m H_0^2\, A^{\mathrm{SZ}} \int dr \Delta^2\!\left(\frac{l_1}{r}\right)\Delta^{2(\mathrm{nl})}
$$

$$
\times\, \left(\frac{l_2}{r}, r\right) g^2 a \dot{G} d_A^8\!\left(\frac{d}{dr}\frac{\dot{F}}{d_A^2}\right). \tag{88}
$$

5.6. Doppler-SZ-OV

Similar to ISW-SZ-OV effect, the hybrid coupling of the reionized Doppler and SZ effects to OV effect. As with the Doppler-Doppler-OV calculation, we integrate the coupling between Doppler effect and OV velocity part and use the Limber approximation to describe the coupling between SZ and OV density part. The bispectrum term is then

$$
b_{l_1,l_2}^{\mathrm{dop}-\mathrm{SZ}} = \frac{16\pi^3}{l_2^3}\, A^{\mathrm{SZ}} \int \frac{dk}{k^2}\, \Delta^2(k) \int dr \Delta^2\!\left(\frac{l_2}{d_A}\right)
$$

$$
\times\, G^2 g^2 a \dot{G} d_A j'_{l_1}(kr) I_{l_1}^{\mathrm{dop}}(k). \tag{89}
$$

As with the other OV-SZ couplings, the nonlinear generalization of the effect is given by

$$
b_{l_1,l_2}^{\mathrm{dop}-\mathrm{SZ(nl)}} = \frac{16\pi^3}{l_2^3}\, A^{\mathrm{SZ}} \int \frac{dk}{k^2}\, \Delta^2(k) \int dr \Delta^{2(\mathrm{nl})}\!\left(\frac{l_2}{d_A}, r\right)
$$

$$
\times\, g^2 a \dot{G} d_A j'_{l_1}(kr) I_{l_1}^{\mathrm{dop}}(k). \tag{90}
$$

5.7. SW-SZ-OV

Finally, we consider a hybrid involving the Sachs-Wolfe (SW) effect at the last scattering surface and the SZ effect. The weight function for the SW effect can be written as

$$
W^{\mathrm{SW}}(k, r_*) = -\frac{\Omega_m H_0^2}{2k^2}\, F \delta^D(r - r_*) \tag{91}
$$

and is evaluated at the last scattering surface, $r_* \approx r_0$. The Limber approximation implies that there is no coupling between the SW effect and the SZ or OV effects because there is no overlap in their weight functions. To the extent, that such a coupling exists the Limber approximation fails.

Since it is at large scales that the Limber approximation breaks down, we are interested in the coupling between OV velocity part and the SW effect. As in the Doppler effects, we use equation (78) to evaluate the deviations from the Limber approximation,

$$
b_{l_1,l_2}^{\mathrm{SW}-\mathrm{SZ}} = -\frac{8\pi^3}{l_2^3}\, \Omega_m H_0^2\, A^{\mathrm{SZ}} F(r_*) j_{l_2}(kr_*) \int \frac{dk}{k^4}\, \Delta^2(k)
$$

$$
\times\, \int_0^{r_0} dr \Delta^2\!\left(\frac{l_2}{r}\right) d_A\, a g^2 \dot{G} G^2 j'_{l_1}(kr) \tag{92}
$$

and its nonlinear analogue

$$
b_{l_1,l_2}^{\mathrm{SW}-\mathrm{SZ(nl)}} = -\frac{8\pi^3}{l_2^3}\, \Omega_m H_0^2\, A^{\mathrm{SZ}} F(r_*) j_{l_2}(kr_*) \int \frac{dk}{k^4}\, \Delta^2(k)
$$

$$
\times\, \int_0^{r_0} dr \Delta^{2(\mathrm{nl})}\!\left(\frac{l_2}{r}, r\right) d_A\, a g^2 \dot{G} j'_{l_1}(kr). \tag{93}
$$

Here we do not consider couplings such as SW-SW-OV effect as the OV density part, with a redshift window at low redshifts, does not couple to SW effect at the last scattering surface.

6. OSTRIKER-VISHNIAC COUPLINGS: RESULTS

In Figure 7 we show χ^2 contributions per logarithmic interval of l_3 for the coupling between linear secondary effects and the OV effect as derived in the previous section. Here we have assumed cosmic variance in the noise only. For the coupling between two secondaries of the same type, the bispectrum contributions per l_3 are substantially smaller than their lensing counterparts (see Fig. 5). An examination of the configuration dependence of the contributions shows that most of the contributions come from triplets, which makes triangles with $l_1 \ll l_2 \lesssim l_3$ (see Fig. 8 for an example). The reason for this behavior is that the OV effect involves the large-scale bulk velocity field and small-scale density fluctuations. One secondary effect couples to the former and one to the latter creating the desired configuration. Because secondary effects tend to be strongly peaked to either small or large angular scales, any coupling involving two secondaries of the same type suffers suppression on one end or the other.

Such configuration dependence also suggests that hybrid couplings should contribute more strongly. In particular in the last section, we considered hybrids composed of one large-scale secondary effect coupling to the OV velocity field and one small-scale secondary effect coupling to the OV density field. As shown in Figure 7, the contribution to the bispectrum produced by the hybrid ISW-SZ coupling is substantially greater than either the ISW-ISW or SZ-SZ couplings. The same is true for the Doppler couplings: Doppler-SZ coupling yields a larger effect than either Doppler-Doppler or SZ-SZ coupling. It is however a smaller contribution than the ISW-SZ coupling.

Except for couplings involving the Doppler effect, the results are fairly insensitive to the reionized optical depth since the others are weighted toward low redshifts. Increasing the optical depth to 0.3 from 0.1, as shown in Figure 7, the Doppler-Doppler-OV effect is increased by factor of ~ 10, and when the optical depth is further increased to ~ 0.5, the Doppler-Doppler-OV contribution becomes comparable to that of the ISW-ISW-OV bispectrum signal at l_3 of a few thousand. The hybrid Doppler-SZ-OV bispectrum is less sensitive to the reionized optical depth than the symmetric Doppler-Doppler-OV coupling, and is below the bispectrum produced by the hybrid ISW-SZ-OV for optical depths to reionization of current interest.

Nonlinearities in the density field can enhance couplings involving the SZ effect. Under the simplifying assumption that the gas density traces the dark matter density, the enhancement in χ^2 for these effects is within a factor of 100, at l_3 of few thousands, which is consistent with the enhancement in the SZ and OV power spectra due to nonlinearities (see Fig. 1), and the behavior of l_1, l_2 and l_3 configurations
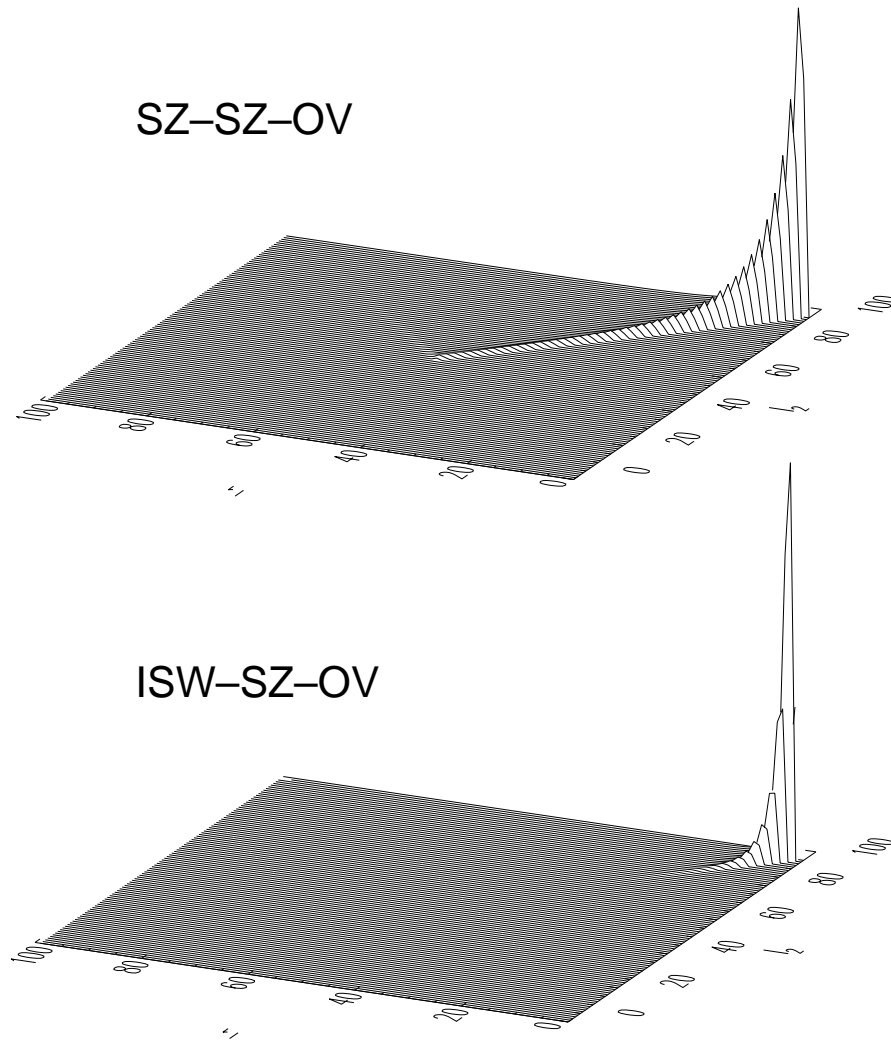
SZ–SZ–OV

ISW–SZ–OV

FIG. 8.—Configuration dependence of the SZ-SZ-OV (*top*) and ISW-SZ-OV (*bottom*) couplings with $l_3 = 100$. This figure is analogous to the one shown in Fig. 6 for secondary-lensing coupling. Contributions generally peak toward $l_3 \sim l_2$ and low l_1 for all l_3-values.

in producing the OV bispectrum. The smaller enhancement factor in the $SZ^{(nl)}$-lensing bispectrum, when compared to secondary-$SZ^{(nl)}$-OV effects, comes from the fact that the secondary-lensing cross-correlation is not enhanced by nonlinear effects out to l of ~ 100 (see, Fig. 5), while the cross-correlation between SZ and density part of the OV effect is even enhanced at very low l-values, as can be seen from Figure 1. One should note that the current calculation using the nonlinear power spectrum should be taken as an estimate of the upper limit of the effects since on the smallest scales gas pressure will make its distribution smoother than that of the dark matter (see discussion in Hu 2000).

In general, Limber approximation when applied to coupling between OV effect and linear sources of anisotropies suggests that coupling only exists for effects with strong temporal overlap in the weight functions W^S and W^{OV}. This suggests that OV coupling with all primary effects, which contribute at $z \sim 1000$ are heavily suppressed. We tested this by numerically integrating the coupling to the SW effect. As shown in Figure 7, the mismatch in redshift between the OV effect and the SW leads to a large suppression of bispectrum signal and the contribution is generally the lowest of all secondary-secondary-OV couplings considered here.

In Figure 9 we study the possible detection of OV-secondary couplings by future satellite CMB missions. Here we have only focussed on the hybrid coupling of ISW and SZ effects to OV effect (ISW-SZ-OV), and its nonlinear analogue ISW-$SZ^{(nl)}$-OV, as they have the largest bispectrum signal of all secondary anisotropies that couple to OV effect. The signal-to-noise ratio generated by such effects is, however, small and their detection is marginal at best even with *Planck*. The ISW-$SZ^{(nl)}$-OV effect has the largest χ^2 with a total value of ~ 2.8 for our fiducial ΛCDM cosmological model. In a flat universe with a cosmological constant, for reasonable variations in Ω_m from 0.2 to 0.7, more or less consistent with current observational constraints on this parameter, the total χ^2 does not vary significantly to make this effect certainly detectable with *Planck*. The variation in χ^2 with Ω_m is such that the largest χ^2-value is ~ 3.1 when $\Omega_m \sim 0.3$ and falls below 1 when $\Omega_m \gtrsim 0.7$ and tends to zero with $\Omega_m \rightarrow 1$; the fall-off is primarily due to the decrease in ISW effect with increasing Ω_m and the ISW effect is zero in an Einstein–de Sitter universe with $\Omega_m = 1$.

Beyond *MAP* and *Planck*, the largest contribution to the signal-to-noise for a perfect experiment comes from l_3-values corresponding to arcminute scales and are at a level that eventual detection may be possible. Even with such a
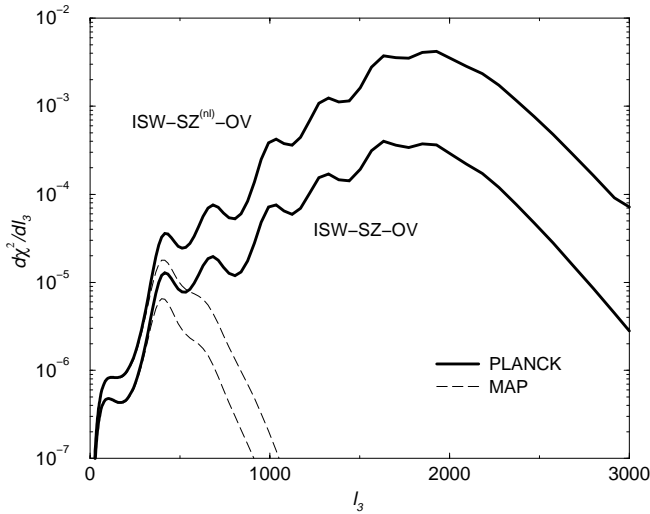
FIG. 9.—Contributions to the χ^2 as a function of l_3 for our fiducial ΛCDM model for ISW-SZ-OV and its nonlinear analogue ISW-SZ$^{(nl)}$-OV with *MAP* and *Planck* noise included in the variance. As shown, the signal-to-noise ratios are generally below the detection level for *MAP* and near or below the threshold for *Planck* ($\chi^2 \sim 0.3,3$ for the linear and nonlinear effects). These effects are the largest of the secondary-OV couplings considered.

high-resolution experiment, one should bear in mind that their detection requires configurations in *l*-space with one short side that picks up contributions from the ISW effect. Its detection perhaps might involve a combination of a small angular scale experiment such as the planned ground-based interferometers and satellite missions that have larger angular coverage. The tight localization of the bispectrum contributions of modulated Doppler effects such as the OV effect is also a useful property from the perspective of their role as a contamination for the secondary-lensing measurements or intrinsic nongaussianity limits. Even if the amplitude is enhanced, say by contributions from the analogous patchy-reionization effect (see § 2.5), a large part of the contamination may be removed by eliminating only a small range in the bispectrum terms.

7. DISCUSSION

Let us summarize the results of this study. Gravitational lensing angular excursions couple with first-order secondary anisotropies generated at reionization to produce a bispectrum in the CMB. Here we have consider the coupling between lensing and the Doppler effect and have shown this to be a significantly smaller effect on the bispectrum than that between lensing and SZ and ISW effects for the low optical depths ($\tau \lesssim 0.3$) expected in adiabatic CDM models. For the currently favored ΛCDM model, under the assumptions made here on the physical state of baryonic gas distribution, the bispectrum produced by SZ-

gravitational lensing angular deflections is generally higher than that produced by ISW-lensing (Goldberg & Spergel 1999). Results from higher resolution hydrodynamic simulations and constraints from observations are clearly needed to improve the calculation associated with SZ effect.

The OV effect couples with two secondary sources of anisotropies to produce a bispectrum. Given that OV effect is due to a product of density and velocity fields, the bispectrum contributions are maximized when one of the secondaries peaks at large angular scales and the other at small angular scales. Such hybrid couplings produce relatively large signals in particular the ISW-SZ-OV effect if the assumptions involved in estimating the SZ contribution prove to be correct. For reasonable models of reionization and currently favored cosmological models, however, the contribution to bispectrum by secondary-secondary-OV coupling is below the level that can be expected to be detected by *MAP* and is marginal at best for *Planck*. Although these signals are unlikely then to be detected in *Planck*, they do serve as a source of residual systematic errors for other measurements of the bispectrum that can grow to be comparable to the cosmic variance term around the arcminute scale. Removal of these contributions is facilitated by the strong localization of these effects at $l_3 \sim l_2$, $l_1 \lesssim 10$. Removal of a broader range of l_1 is undesirable since many of the interesting bispectrum effects are also maximized for $l_3 \sim l_2$.

In general, bispectrum contributions from the coupling of secondary anisotropies depends not only on the intrinsic amplitude of the secondary effects but also their overlap in redshift. In the small-scale Limber approximation, only equal time correlations contribute. Many of the effects considered here are substantially smaller than one would naively guess, owing to mismatch in the epochs at which the effects contribute their signal.

We have considered contributions to the CMB bispectrum from reionization to leading order in the density fluctuations. This is appropriate for the angular scales probed by the upcoming satellite missions. On arcminute scales and below, CMB anisotropies will be dominated by contributions from truly nonlinear structures in the gas density, temperature, and ionization state. The nongaussianity induced on these quantities by structure formation will be a rich field for future studies as experiments begin to probe the subarcminute regime of CMB anisotropies.

APPENDIX A

USEFUL PROPERTIES OF THE WIGNER-3*j* SYMBOL

Here we review the properties of the Wigner-3*j* symbol that are useful for the derivations in the text. It is defined by its relation to the Clebsch-Gordan coefficient,

$$\begin{pmatrix} l_1 & l_2 & l_3 \\ m_1 & m_2 & m_3 \end{pmatrix} = (-1)^{l_1 - l_2 - m_3} \frac{\langle l_1 m_2, l_2 m_2 | l_3 - m_3 \rangle}{(2l_3 + 1)^{1/2}} . \tag{A1}$$

As a consequence it obeys the orthonormality relation

$$\sum_{m_1 m_2} \begin{pmatrix} l_1 & l_2 & l_3 \\ m_1 & m_2 & m_3 \end{pmatrix} \begin{pmatrix} l_1 & l_2 & l_4 \\ m_1 & m_2 & m_4 \end{pmatrix} = \frac{\delta^{\mathrm{D}}_{\ell_3 \ell_4} \delta^{\mathrm{D}}_{m_3 m_4}}{2\ell_3 + 1} , \tag{A2}$$

the even permutation relation

$$\begin{pmatrix} l_1 & l_2 & l_3 \\ m_1 & m_2 & m_3 \end{pmatrix} = \begin{pmatrix} l_2 & l_3 & l_1 \\ m_2 & m_3 & m_1 \end{pmatrix} = \begin{pmatrix} l_3 & l_2 & l_1 \\ m_3 & m_2 & m_1 \end{pmatrix} 321 , \tag{A3}$$

and the odd permutation relation

$$\begin{pmatrix} l_1 & l_2 & l_3 \\ m_1 & m_2 & m_3 \end{pmatrix} = (-1)^L \begin{pmatrix} l_2 & l_1 & l_3 \\ m_2 & m_1 & m_3 \end{pmatrix} , \tag{A4}$$

where $L = l_1 + l_2 + l_3$. Given symmetry under spatial inversions only bispectrum terms with even L are nonzero. Since parity forces L to be even, all permutations and negation of the m-values are equal. Furthermore, the angular momentum selection rules require $l_i \le |l_j - l_k|$ for all permutations of the indices, and $m_1 + m_2 + m_3 = 0$.

From the Clebsch-Gordan relation and series one can derive the integral relation to spherical harmonics,

$$\int d\hat{n} \, Y^{m_1}_{l_1} Y^{m_2}_{l_2} Y^{m_3}_{l_3} = \sqrt{\frac{(2l_1 + 1)(2l_2 + 1)(2l_3 + 1)}{4\pi}} \begin{pmatrix} l_1 & l_2 & l_3 \\ 0 & 0 & 0 \end{pmatrix} \begin{pmatrix} l_1 & l_2 & l_3 \\ m_1 & m_2 & m_3 \end{pmatrix} . \tag{A5}$$

From conjugation of this relation, one finds that

$$\begin{pmatrix} l_1 & l_2 & l_3 \\ m_1 & m_2 & m_3 \end{pmatrix} = (-1)^L \begin{pmatrix} l_1 & l_2 & l_3 \\ -m_1 & -m_2 & -m_3 \end{pmatrix} . \tag{A6}$$

For $m_i = 0$, the Wigner-3j symbol can be efficiently evaluated

$$\begin{pmatrix} l_1 & l_2 & l_3 \\ 0 & 0 & 0 \end{pmatrix} = (-1)^{L/2} \frac{(\frac{L}{2})!}{(\frac{L}{2} - l_1)!(\frac{L}{2} - l_2)!(\frac{L}{2} - l_3)!} \left[\frac{(L - 2l_1)!(L - 2l_2)!(L - 2l_3)!}{(L + 1)!} \right]^{1/2} \tag{A7}$$
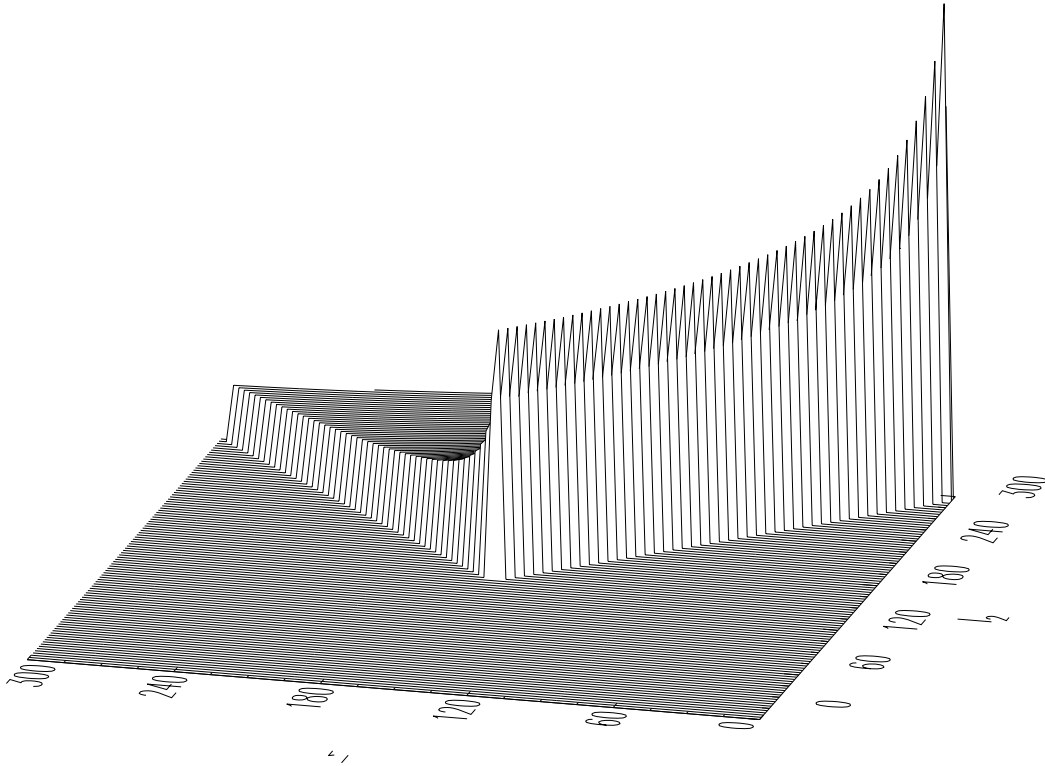

Fig. 10.—Absolute value of the Wigner-3j symbol for $m_i = 0$ as a function of l_1 and l_2 when $l_3 = 300$. We plot only even $l_1 + l_2 + l_3$.

for even L; it vanishes for odd L. In Figure 10 we show the absolute value of the Wigner 3-j symbol when $m_i = 0$ as given above. This expression is encountered in all our calculations on the bispectra produced by secondary effects. Note that other Wigner 3j terms, especially when m_i is not equal to zero may be efficiently evaluated through recursion relations and the WKB approximation at high multipole argument (Schulten & Gordon 1975).

REFERENCES

Aghanim, N., Desert, F. X., Puget, J. L., & Gispert, R. 1996, A&A, 311, 1
Banday, A. J., Zaroubi, S., & Gorski, K. M. 1999, ApJ, in press (astro-ph/9908070)
Bromley, B., & Tegmark, M. 1999, ApJ, 524, L79
Bunn, E. F., & White, M. 1997, ApJ, 480, 6
Carlstrom, J. E., Joy, M., & Grego, L. 1996, ApJ, 456, L75
Cen, R., & Ostriker, J. P. 1999, ApJ, 514, 1
da Silva, A. C., Barbosa, D., Liddle, A. R., & Thomas, P. A. 1999, MNRAS, submitted, astro-ph/9907224
Eisenstein, D. J., & Hu, W. 1999, ApJ, 511, 5
Falk, T., Rangarajan, R., & Frednicki, M. 1993, ApJ, 403, L1
Ferreira, P. G., Magueijo, J., & Gorksi, K. M. 1998, ApJ, 503, 1
Gangui, A., Lucchin, F., Matarrese, S., & Mollerach, S. 1994, ApJ, 430, 447
Gangui, A., & Martin, J. 2000, MNRAS, 313, 323
Goldberg, D. M., & Spergel, D. N. 1999, Phys. Rev. D, 59, 103002
Griffiths, L. M., Barbosa, D., & Liddle, A. R. 1999, MNRAS, 308, 845
Gruzinov, A., & Hu, W. 1998, ApJ, 508, 435
Haiman, Z., & Knox, L. 1999, in ASP Conf. Ser. 181, Microwave Fore-grounds, ed. A. de Oliveira-Costa & M. Tegmark (ASP: San Fransisco), astro-ph/9902311
Heavens, A. 1998, MNRAS, 299, 805
Hinshaw, G., Banday, A. J., Bennett, C. L., Gorski, K. M., & Kogut, A. 1995, ApJ, 446, 67
Hu, W. 2000, ApJ, 529, 12
Hu, W., & White M. 1996, A&A, 315, 33
Kaiser, N. 1984, ApJ, 282, 374
———. 1992, ApJ, 388, 286

Kendall, M. G., & Stuart, A. 1969, Advanced Theory of Statistics, Vol. II (London: Griffin)
Knox, L. 1995, Phys. Rev. D, 48, 3502
Knox, L., Scoccimarro, R., & Dodelson, S. 1998, Phys. Rev. Lett., 81, 2004
Limber, D. 1954, ApJ, 119, 655
Luo, X. 1994, ApJ, 1994, ApJ, 427, 71
Luo, X., & Schramm, D. N. 1993, Phys. Rev. Lett., 71, 1124
Ostriker, J. P., & Vishniac, E. T. 1986, Nature, 322, 804
Pando, J., Vallas-Gabaud D., & Fang, L. 1998, Phys. Rev. Lett., 79, 1611
Peacock, J. A., & Dodds, S. J. 1996, MNRAS, 280, L19
Peebles, P. J. E. 1980, The Large-Scale Structure of the Universe, (Princeton: Princeton Univ. Press)
Rees, M. J., & Sciama, D. N. 1968, Nature, 519, 611
Sachs, R. K., & Wolfe, A. M., 1967, ApJ, 147, 73
Schulten, K. & Gordon, R. G. 1975, J. Math. Phys., 16, 1971
Seljak, U. 1996, ApJ, 460, 549
Seljak, U., & Zaldarriaga, M. 1996, ApJ, 469, 437
———. 1999, Phys. Rev. D. 60, 043504
Spergel, D. N., & Goldberg, D. M. 1999, Phys. Rev. D, 59, 103001
Sunyaev, R. A. & Zel'dovich, Ya. B. 1980, MNRAS, 190, 413
Tegmark, M., Eisenstein, D. J., Hu, W., & de Oliveira-Costa, A. 1999, ApJ, 530, 133
Vishniac, E. T. 1987, ApJ, 322, 597
Wang, L., & Kamionkowski, M. 2000, Phys. Rev. D., 60, 063504
White, M., Carlstrom, J. E., Dragovan, M., & Holzapfel, W. L. 1999, ApJ, 514, 12
Zaldarriaga, M., & Seljak, U. 1997, Phys. Rev. D, 55, 1830